Surface area-enhanced cerium and sulfur-modified hierarchical bismuth oxide nanosheets for electrochemical carbon dioxide reduction to formate.

PALANTIMUTHU, N., SUBRAMANIAM, M.R., P, M.A., SHARMA, P.K., RAMALINGAM, V., PERAMAIAH, K., RAMAKRISHNAN, S., GU, G.H., YU, E.H. and YOO, D.J.

2024

Surface Area-Enhanced Cerium and Sulfur-Modified Hierarchical Bismuth Oxide Nanosheets for Electrochemical Carbon Dioxide Reduction to Formate

Naveenkumar Palanimuthu,[1] Mohan Raj Subramaniam,[1] Muthu Austeria P.,[2] Preetam Kumar Sharma,[3,4] Vinoth Ramalingam,[5] Karthick Peramaiah,[6] Shanmugam Ramakrishnan,[7] Geun Ho Gu,[2] Eileen Hao Yu,[4] Dong Jin Yoo,[1,8,]

1 Graduate School, Department of Energy Storage/Conversion Engineering (BK21 FOUR), Hydrogen and Fuel Cell Research Center, Jeonbuk National University, Jeonju, Jeollabuk-do, 54896, Republic of Korea
2 Department of Energy Engineering, Korea Institute of Energy Technology (KENTECH), Naju, 58330, Republic of Korea
3 Institute for Materials Discovery, University College London, Malet Place, London, WC1E 7JE, UK
4 Department of Chemical Engineering, Loughborough University, Loughborough, LE11 3TU, UK
5 School of Engineering, Robert Gordon University, Garthdee Road, Aberdeen, AB10 7GJ, UK
6 Agency for Science, Technology, and Research, Institute of Sustainability for Chemicals, Energy and Environment, Singapore, 138634, Singapore
7 School of Engineering, Newcastle University, Merz Court, Newcastle upon Tyne, NE17RU, UK
8 Department of Life Science, Jeonbuk National University, Jeonju, Jeollabuk-do, 54896, Republic of Korea
E-mail: djyoo@jbnu.ac.kr

Jeonbuk National University Research
Ministry of Education : 2023RIS-008
National Research Foundation of Korea Ministry of Science, ICT and Future Planning : NRF-2020R1A2B5B01001458
UK Research and Innovation : EP/V011863/1

Abstract
Electrochemical carbon dioxide reduction reaction (ECO_2RR) is a promising approach to synthesize fuels and value-added chemical feedstocks while reducing atmospheric CO_2 levels. Here, high surface area cerium and sulfur-doped hierarchical bismuth oxide nanosheets (Ce@S-Bi_2O_3) are developed by a solvothermal method. The resulting Ce@S-Bi_2O_3 electrocatalyst shows a maximum formate Faradaic efficiency of (FE) 92.5% and a current density of 42.09 mA cm^{-2} at −1.16 V versus RHE using a traditional H-cell system. Furthermore, using a three-chamber gas diffusion electrode (GDE) reactor, a maximum formate FE of 85% is achieved in a wide range of applied potentials (−0.86 to −1.36 V vs RHE) using Ce@S-Bi_2O_3. The density functional theory (DFT) results show that doping of Ce and S in Bi_2O_3 enhances formate production by weakening the OH* and H* species. Moreover, DFT calculations reveal that *OCHO is a dominant pathway on Ce@S-Bi_2O_3 that leads to efficient formate production. This study opens up new avenues for designing metal and element-doped electrocatalysts to improve the catalytic activity and selectivity for ECO_2RR.

Keywords
bismuth oxide; density functional theory; electrochemical CO2 reduction; formate; surface area

1. Introduction

Increasing atmospheric carbon dioxide (CO_2) levels from fossil fuel combustion and industrial activities is one of the most important global climate challenges.[1] Carbon capture and utilization technologies represent a potential solution for mitigating the CO_2 levels in the atmosphere.[2] Electrochemical CO_2 reduction (ECO_2RR) is a promising strategy to transform CO_2 into a wide range of useful fuels and chemicals such as carbon monoxide, methane, formate, methanol, and ethanol.[3] Among various CO_2-reductant products, formate is considered one of the most valuable products. Formate is an essential feedstock for the pharmaceutical industry, a hydrogen (H_2) energy carrier for fuel cells, and fuel for direct electricity generation with high economic benefits.[4] Based on previously reported studies, several metal-based catalysts (e.g., Pd, In, Sn, Bi, Pb, Tl, Hg, and Cd), and metal oxides (e.g., In_2O_3, SnO_2, Bi_2O_3, and CuO) have been reported to convert CO_2 to formate through ECO_2RR.[5] However, many heavy metals (Pb, Cd, Hg, and Tl) are highly toxic and environmentally hazardous and are not recommended for practical applications.[6] In this regard, Bi-based electrocatalysts have been widely investigated due to their non-toxic nature, low-cost effectiveness, and earth abundance.[7]

Bi-based materials such as Bi_2O_3[8] and Bi_2S_3[9] have gained significant attention for their efficiency and selectivity in converting CO_2 to formate. However, most of these Bi electrocatalysts have limited activity (current density <40 mA cm^{-2}) and low selectivity for formate (< 80%) due to the significance of H_2 evaluation at higher current densities.[10] Numerous strategies have been introduced for Bi_2O_3 catalyst design to improve the activity and selectivity of ECO_2RR, such as nanostructures,[11] crystal facet control,[12] defect engineering,[13] tailoring the band structure,[14] metal doping,[15] and use with other materials. Based on that, modified Bi_2O_3 hierarchical nanostructures have recently gained widespread acceptance due to their excellent catalytic performance.[16] Specifically, the nanostructure has a large specific surface area and abundant active sites that interact with the reactants and promote catalytic activity. The hierarchical nanostructure surfaces with high indices contain many coordinately unsaturated sites, edge sites, and structural defects, which play a crucial role in stabilizing key *OCHO intermediate species.[17] This stabilization mechanism enhanced the catalytic activity of the Bi site, leading to increased production of formate.[18]

Moreover, modifying the electron density of the catalytic active site through heteroatom doping can further improve the catalytic efficiency of these nanostructures.[19–22] Specifically, the doped heteroatoms (such as N and S) can regulate the electron density of the catalyst, which modifies the electronic configurations of active sites to achieve the ideal adsorption energy with reaction intermediates for formate production in ECO_2RR.[23] For instance, sulfur (S) doping creates a large number of oxygen vacancies and increases the adsorption intensity of CO_2, which could enhance the electrocatalytic activity.[24] Similarly, metal atom doping in Bi_2O_3 electrocatalysts has been explored for the ECO_2RR to formate.[21,25,26] The inclusion of metal dopants can accelerate the charge transfer within the electrocatalyst, a crucial factor for optimizing the efficiency of electrochemical reactions and elevating reaction rates.[27] Metal doping has a role in modifying the electronic structure and surface defects, which is beneficial for producing formate in ECO_2RR.[28] Recently, rare-earth-doped Bi_2O_3 was used in ECO_2RR. Yan et al., demonstrated that Eu-Bi doping resulted in enhanced selectivity and stability in a wide range of potentials in ECO_2RR.[29] In a separate study, Zhou et al., demonstrated these benefits in the bimetal Ag-Bi-S-O catalyst, achieving exceptional formate selectivity >94% FE and a 12.5 mA cm^{-2} current density with a wide range of potentials in ECO_2RR.[30] Recently, the modified metal S-O has proved to be a better electrocatalyst for formate production in ECO_2RR.[31] Furthermore, the selectivity in electrochemical CO_2 reduction depends on the relative confinement of the reaction intermediates (*OCHO, *HCOOH,*CO, and *H2) on the surface.[32] In this regard, modification strategies for optimizing the binding of intermediates on the electrocatalysts surface are essential for improving ECO2RR performance.[33]

In this work, we report the synthesis of Ce and S-modified hierarchical nanosheet Bi_2O_3 electrocatalysts for the ECO_2RR. The combined effect of Ce and S-doping, along with unique hierarchical nanosheet morphology, significantly enhances formate production. The prepared Ce@S-Bi_2O_3 electrocatalyst displays Faradaic efficiency of formate ($FE_{formate}$) > 90% in a wide potential window (−0.76 to −1.36 V vs RHE) in both analyzed H-cell and GDE reactor methods. Further, the density functional theory (DFT) calculations demonstrated the presence of Ce@S-Bi_2O_3 and showed that the S and Ce modification reduced the energy barrier for forming the key *OCHO intermediate, resulting in a highly optimized ECO_2RR. This study offers a simple and effective strategy to design metal and heteroatom- doped Bi_2O_3 electrocatalysts for ECO_2RR.

2. Results and Discussion

2.1 Structural Evaluation of the Synthesized Catalyst

Figure 1a illustrates a schematic representation of Ce@S-Bi_2O_3 hierarchical nanosheet synthesis through a one-step solvothermal process. During the reaction process Bi^{3+} ions in the metal precursor react with thioacetamide (S^{2-}) ions and Ce^{3+} ions to form hierarchical nanosheets of Ce@S-Bi_2O_3.[34] Briefly, bismuth (III) nitrate, cerium (III) nitrate, and thioacetamide were dissolved in a 1:2 ratio of ethylene glycol (EG) and ethanol solvent. The homogeneous solution was treated at 170 °C for 6 h by a solvothermal method. Bi_2O_3 and S-Bi_2O_3 electrocatalysts were synthesized through a similar method. The prepared catalysts were used for ECO_2RR.

Figure 1

Synthesis and morphological characterization of the Ce@S-Bi_2O_3 electrocatalyst. Figure 1, a) Schematic illustration of the Ce@S-Bi_2O_3 catalyst synthesis process. b,c) FE-SEM images of Ce@S-Bi_2O_3 demonstrate the hierarchical nanosheet morphology. d) TEM images of Ce@S-Bi_2O_3 show that the hierarchical nanosheet. e,f) HR-TEM images and SAED pattern with crystal planes (111) of Ce@S-Bi_2O_3 hierarchical nanosheet.

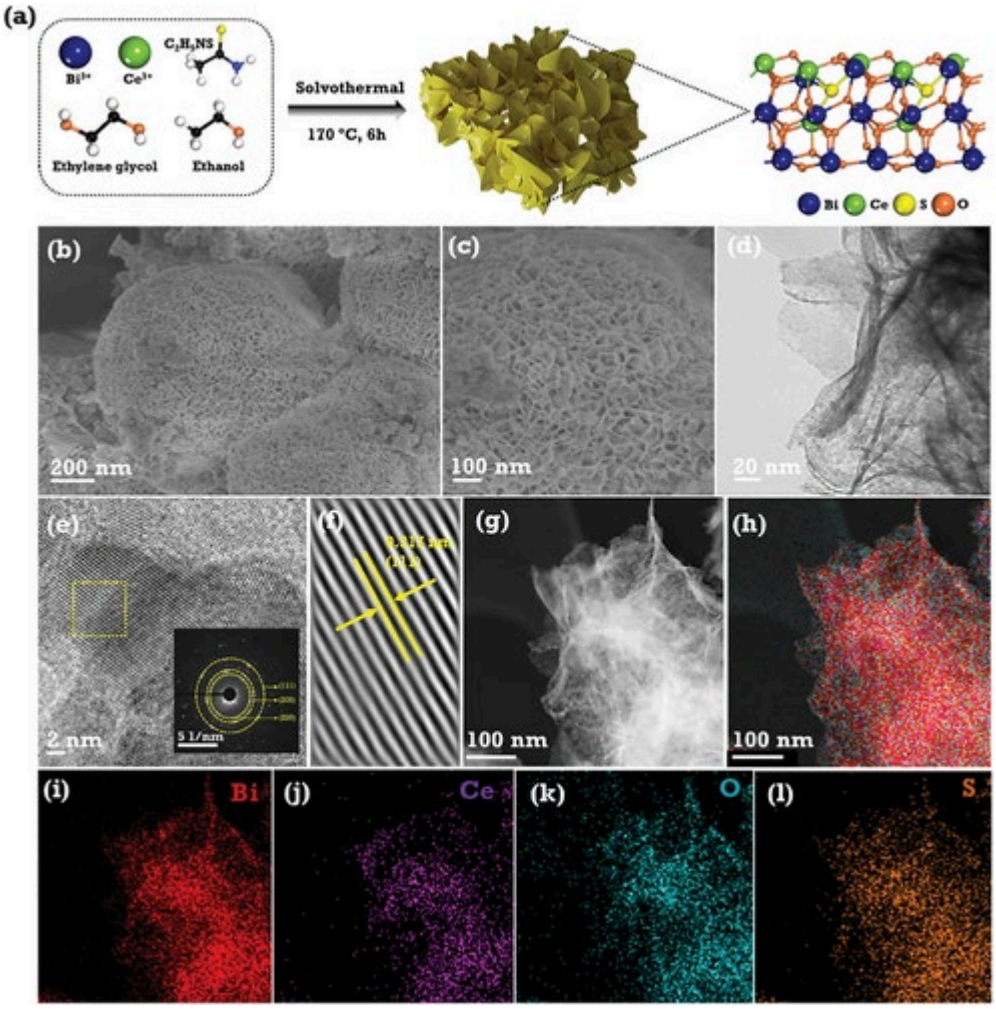

The morphology of the prepared catalysts was analyzed using FE-SEM technique. Figures S1 and S3 (Supporting Information) shows the FE-SEM images of Bi_2O_3, S-Bi_2O_3, and Ce@S-Bi_2O_3 catalysts and their corresponding energy dispersive X-ray spectroscopy (EDS) element maps. This reveals the formation of a 2–3 μm average size hierarchical microsphere structure in all synthesized catalysts with uniform distribution of the Bi, Ce, S, and O elements. Figure 1b,c shows an FE-SEM image of the Ce@S-Bi_2O_3 catalyst, which confirmed the formation of a hierarchical nanosheet structure upon addition of Ce and S with bare Bi_2O_3. Moreover, magnified FE-SEM images (Figure 1c) elucidated the origin of hierarchical microsphere growth, which occurred by assembling a hierarchical nanosheet structure with a uniform spacing of 102.1 ± 21.7 nm. Further, the nanosheet assembly thickness was measured using ImageJ software and was in the range of 10.41 ± 3.05 nm. During the solvothermal reaction, EG unambiguously directs the formation of a hierarchical nanosheet of Bi_2O_3 due to its chelating ability.[35] When $Bi(NO_3)_2{\cdot}5H_2O$ and $Ce(NO_3)_2{\cdot}6H_2O$ are dissolved in EG, they chelate with glycols and form a respective alkoxide. Moreover, the

formation of these alkoxides can reduce the concentration of Bi^{3+} and Ce^{3+} ions in solution to form a uniform hierarchical nanosheet.[36] This phenomenon effectively prevents aggregation, facilitating the growth of even, well-defined hierarchical nanosheets with controlled thickness and desired properties. Furthermore, inductively coupled plasma-optical emission spectroscopy (ICP-OES) results reveal the doping percentages of Ce (3.3 at%) and S (1.2 at%) in the prepared Ce@S-Bi_2O_3 catalysts, which agree with the EDS results from FE-SEM (Figure S3c, Supporting Information). We performed transmission electron microscopy (TEM) and high-angle annular dark field scanning TEM (HADDF-STEM) analysis to understand the hierarchical nanosheet formation in Ce@S-Bi_2O_3. The TEM image (Figure 1d) elucidates the presence of folded, nanosheet assemblies of Ce@S-Bi_2O_3 electrocatalyst. A magnified TEM image (Figure S4b, Supporting Information) displays the formation of hierarchical nanosheets by orderly connected Ce and Bi nanoparticles, which induce the formation of a large nanosheet assembly. Some of the nanosheets were partially folded, and the fold lines exhibited darker features due to the accumulation of dense Bi and Ce metal nanoparticles, which led to the formation of hierarchical nanosheets.[37] An HR-TEM image (Figure 1e) shows the presence of highly crystalline catalysts with clear lattice fringes all over the catalysts. The associated FFT (fast Fourier transform) image shown in Figures 1f and S4 (Supporting Information) obtained from the HR-TEM image indicates that the obtained lattice fringes were related to the (111) plane with an interplanar spacing of 0.318 nm, which matches the formation of Bi_2O_3 (JCPSD: 27–0052).[38] Notably, (HAADF-STEM) examination showed that these distinct nanosheet interactions and overlapping interactions were largely consistent, leading to the formation of foldable nanoparticles attached to the surface of hierarchical nanosheets represented in Figure 1g,h.[24] However, some discontinuities might exist in the inherited lattice defects, while oxide layers appeared due to partial oxidation of the Bi catalyst.[39] STEM-EDS mapping demonstrated the uniform distribution of Bi and Ce and S, O elements along the hierarchical nanosheet as represented in Figure 1i–l, and (Figure S5, Supporting Information). The hierarchical nanosheets provide a platform for efficient CO_2 conversion by providing a larger number of active site and enhanced mass transport so it is more beneficial for catalytic activity surfaces in Ce@S-Bi_2O_3 electrocatalysts. Moreover, the hierarchical nanosheet structure enhances catalytic performance by exposing a substantial surface area with numerous active sites and enabling easy electrolyte penetration and diffusion in electrochemical activity.[40] Also, HAADF-STEM shows a hierarchical nanosheet folded edge in the image (Figure S6, Supporting Information). These Bi_2O_3 nanosheets exposed large quantities of nanoparticles arranged in nanosheets.[37,41] This is accompanied by breaking of Bi─O bonds and the formation of Bi nanosheets. As a result, structural defects in bismuth can significantly improve its electrochemical performance.[39,42] Moreover, Brunauer–Emmett–Teller (BET) surface area measurements of the synthesized Bi_2O_3, S-Bi_2O_3, and Ce@S-Bi_2O_3 (obtained using a Microtrac, BELsorp-mini II) from nitrogen-adsorption-desorption isotherms are shown in Figure S7a–c (Supporting Information). The hierarchical nanosheets of sulfur-modified S-Bi_2O_3 and Ce@S-Bi_2O_3 exhibited high surface areas of (44.01 $m^2\ g^{-1}$) and (50.48 $m^2\ g^{-1}$) compared to undoped Bi_2O_3 (30.40 $m^2\ g^{-1}$). The abruptly improved surface area (>40%) would be expected to improve catalyst reaction kinetics during the ECO_2RR. The high-surface-area mesoporous S-doped Bi_2O_3 might be due to the presence of SO_x gases evolved during the solvothermal reactions with addition sulfur source (C_2H_5NS).[43] Further, the obtained mesoporous pore diameter (21.52 nm) and enhanced pore volume (0.2716 cm^3g^{-1}) (inset Figure S7a–c and

Table S1, Supporting Information) clearly revealed the formation of highly active Ce@S-Bi_2O_3 porous materials in this reaction. All the all active sites in Bi are available to the reactant due to the high mesoporosity, which could enhance charge transfer rate during the electrochemical reaction.[34].

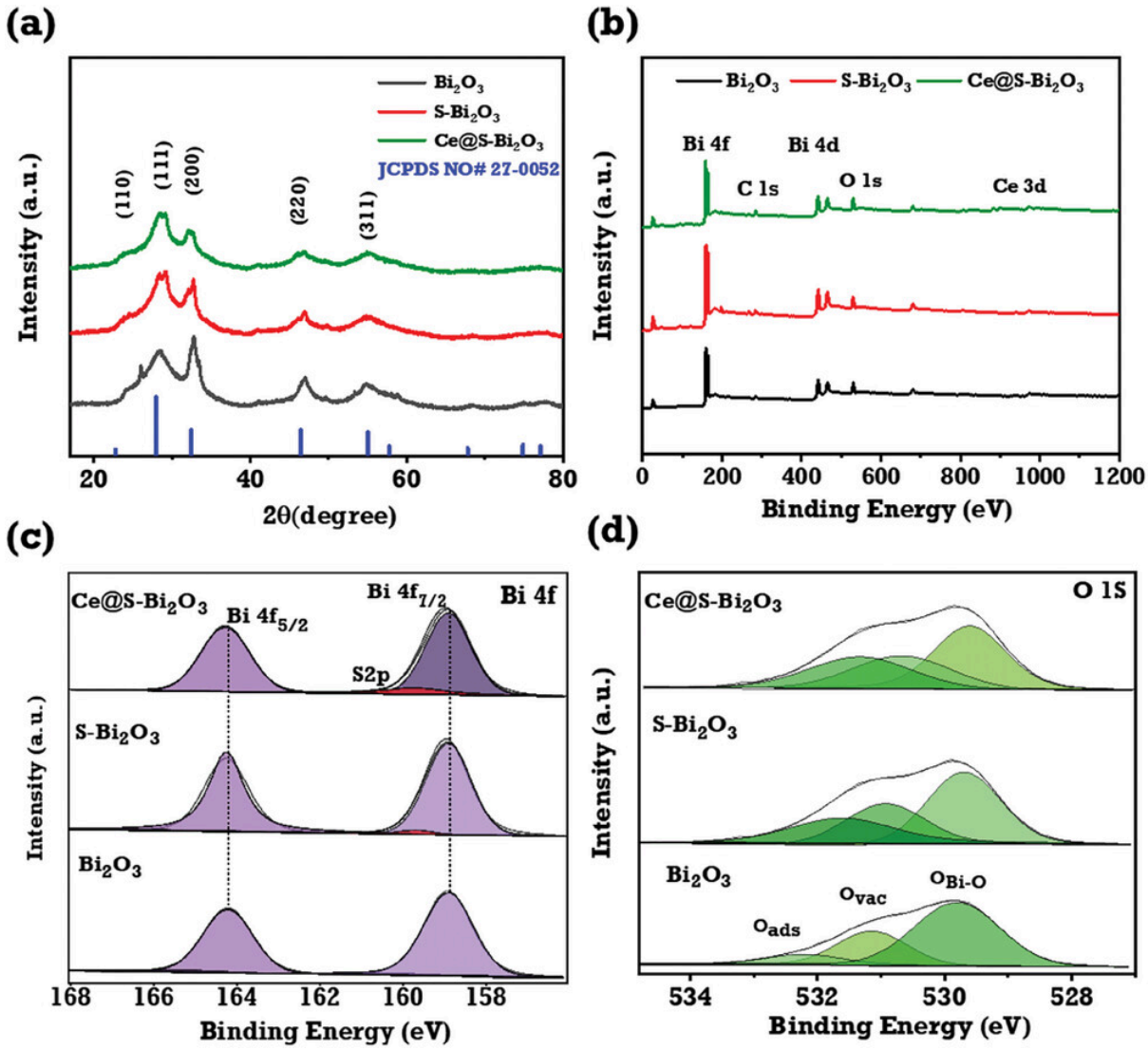

Figure 2

Crystal structure and chemical states of the attained (Ce@S-Bi_2O_3) electrocatalyst. a) XRD patterns of Bi_2O_3, S-Bi_2O_3, and Ce@S-Bi_2O_3 of electrocatalysts. b) High-resolution survey spectrum of (Bi_2O_3, S-Bi_2O_3, and Ce@S-Bi_2O_3 electrocatalyst). c) High-resolution XPS spectra of Bi 4f. d) O1s XPS spectrum of Bi_2O_3, S-Bi_2O_3, and Ce@S-Bi_2O_3 electrocatalyst.

The crystal patterns of the synthesized Bi_2O_3 hierarchical nanosheets were determined by XRD analysis (Figure 2a). Diffraction peaks noted at 22.74°, 27.94°, 32.38°, 46.44°, and 55.08° correspond to (1 1 0), (1 1 1), (2 0 0), (2 2 0), and (3 1 1) lattice planes, respectively, which confirmed that the prepared Bi_2O_3 had a cubic phase with a space group Pn3m.[28] The predominant peak ≈27.94° corresponds to the (111) plane of Bi_2O_3. The observed XRD results agree with the JCPDS number of 27–0052, indicating the formation of the cubic phase α-Bi_2O_3.[38] Moreover, after undergoing S-doping, the peaks became broader. These specific

changes can be attributed to the reduced crystallinity. This indicates that the S modification led to a less ordered and reduced crystallite size in te S-Bi_2O_3 electrocatalyst. Apart from α-Bi_2O_3 phase, no additional peaks appeared in S-Bi_2O_3, suggesting the existence of either a small proportion or amorphous nature of S within the S-Bi_2O_3 electrocatalyst. [43b] Furthermore, the electrochemical study indicates the enhanced catalytic activity of the amorphous nature of S-doped Bi_2O_3 compared to the undoped electrocatalyst. Moreover, when S was added to Bi_2O_3, the peaks in the crystal structure were separated, possibly due to S having a similar lattice parameter to α-Bi_2O_3. This analysis further confirmed the importance of S-doping in the Bi_2O_3 nanostructures. The slight positive shift of 2θ ensures the incorporation of Ce in S-Bi_2O_3.[44] No diffraction reflections other than those for α-Bi_2O_3 were detected, which indicated the formation of a highly pure α-Bi_2O_3 phase.

Furthermore, X-ray photoelectron spectroscopy (XPS) measurements were carried out to investigate the elemental compositions and chemical states of Bi_2O_3, S-Bi_2O_3, and Ce@S-Bi_2O_3 electrocatalyst as shown in Figure 2b. Figure 2c presents the Bi $4f_{7/2}$ and Bi $4f_{5/2}$ peak pair at 159.0 and 164.2 eV for Bi_2O_3, which was ascribed to Bi species. Compared to as-synthesized Bi_2O_3, a positive shift of approximately 0.3 eV was observed for the Ce@S-Bi_2O_3 electrocatalyst.[45] The XPS peak corresponding to S2p peak 159.8 eV shifts slightly toward higher binding energies, indicating enhanced S bond strength. This observation is highlighted the ability of heteroatom doping to effectively modulate the bonding strength of materials.[46] Additionally, the S-doped Bi_2O_3 spectrum has a peak between core Bi at 159.7 eV. For S-Bi_2O_3 a slight peak of Bi $4f_{7/2}$ was observed and was assigned to S^{2-} in sulfides.[47] This suggests that S was present at the weaker O sites of Bi_2O_3, resulting in S bonding with the Bi site (Bi-S). Furthermore, the incorporation of S was shifted to 0.3 eV. Moreover, the Ce^{3+} ions and oxygen vacancy sites were located on the surface of Ce. The Ce@S-Bi_2O_3 showed a positive shift of 0.18 eV in the Bi sites compared with Bi_2O_3, indicating partial charge from Bi to Ce, and the electronic structure of Bi was tuned by the strong interaction with Ce.[45] Figure S8 (Supporting Information) shows the deconvoluted Ce 3d core level spectrum, which revealed the valence states of both the Ce^{3+} and Ce^{4+} multiple d-splitting such as $3d_{3/2}$ and $3d_{5/2}$. The characteristic peaks of the mixed valence, such as Ce^{4+} $3d_{5/2}$ and Ce^{4+} $3d_{3/2}$, were located at binding energies of 916.7 and 898.6 eV, respectively. The Ce^{3+} ions consist of peaks located at binding energies of 901.6 and 881.3 eV, which were assigned to Ce^{3+} $3d_{3/2}$ and Ce^{3+} $3d_{5/2}$, respectively.[48] The mixed states of Ce ions were also indicated by additional satellite peaks (orbital "shake-up") located at 06.8 eV for Ce^{3+} $3d_{3/2}$ and 885.3 and 889.2 eV for Ce^{3+} $3d_{5/2}$.[49,50] The Ce 3d spectrum indicates that the concentration of Ce^{3+} ions increased, and their lattice parameters expanded because of the reduced electrostatic force derived from the increased concentration of Ce^{3+} ions. This result indicates the presence of Ce^{3+}, which could include O-vacancies.[51–53] A decrease in lattice oxygen intensity was observed in the S and Ce-doped Bi_2O_3 electrocatalyst.

The O1s spectrum of the Bi_2O_3 and S-Bi_2O_3 and Ce@S-Bi_2O_3 catalyst can be deconvoluted into three peaks denoted as Bi-O bond (O_{lat}), an oxygen vacancy (O_{vac}), and adsorbed oxygen (O_{ads}) characteristics of oxygen atoms bonded to metals peaks at 529.8, 529.7, and 529.6 eV, respectively. Interestingly, the characteristic peaks of Ce@S-Bi_2O_3 shown at 531.1, 530.9, and 530.7 eV (O_{vac}) decreased compared to those of S- Bi_2O_3 at 530.7 eV. The high concentrations of O-vacancies and Ce^{3+} ions may enhance the electrocatalytic selectivity for facilitated adsorption of CO_2 with O-bonding.[51a] The adsorbed oxygen (O_{ads}) peaks are located at 532.1, 531.6, and 531.3 eV in Bi_2O_3, S-Bi_2O_3, and Ce@S-Bi_2O_3 catalyst, respectively, and the oxygen vacancy peak of 530.7 eV can be ascribed to the presence of Ce@S-Bi_2O_3 as

shown in Figure 2d. Furthermore, Fourier transform infrared (FTIR) and Raman spectroscopy analysis were performed to understand the surface properties of the Ce@S-Bi_2O_3 catalyst. The FTIR spectra of Ce@S-Bi_2O_3 shows the peaks at 400 to 600 cm^{-1} and 1047. 1355, 2159, and 2972 cm^{-1} are the characteristic groups of Bi─O, respectively (Figure S9a, Supporting Information).[54] The peak at 3380 cm^{-1} belongs to the adsorbed water and surface hydroxyl peaks O─H, extending vibrations over the surface of the electrocatalyst.[55] Furthermore, the peak edge at 879 cm^{-1} is assigned to the Bi─O─C bending vibrations of Bi_2O_3 in the presence of air adsorbed.[56] In addition, the Raman characteristic bands at ≈980 to 1200 cm^{-1} are ascribed to the doping of S presence in Bi─O. The band broadening at ≈731 and 1046, 1248, and 1571 cm^{-1} belongs to Ce-O.[45,57] Hence, it is confirmed that incorporating S and Ce changes the surface area of the Bi_2O_3 nanosheet. To further understand the structure of the catalyst, we performed Raman analysis Figure S9b (Supporting Information). The peaks noted at 149192 and 307 cm^{-1}corresponds to the Bi─O outline representing various bending and, stretching modes in the Bi_2O_3 nanosheet.[58] From the spectrum, the slight peak present in 465 cm^{-1} represents the Ce─O and, further the broad, penetrating peaks ≈437 cm^{-1} are typical peaks of Ce─O.[59] In addition, the peak observed at 254 and 970 cm^{-1} is attributed to the S in Bi_2O_3 nanosheet.[60]

2.2 Electrochemical CO_2 Reduction Reactions

Electrochemical CO_2RR was carried out using an H-cell, as illustrated in Figure 3a. Further the Figures 3b and S10 (Supporting Information) show the linear sweep voltammetry (LSV) curves of Bi_2O_3, S-Bi_2O_3, and Ce@S- Bi_2O_3 electrocatalysts in N_2 and CO_2-saturated 0.5 M $KHCO_3$ electrolyte with a scan rate of 5 mV s^{-1}. The current density obtained for all three electrocatalysts in the CO_2-saturated electrolyte was significantly higher than that in N_2-saturated conditions, which shows efficient ECO_2RR activity.[61] Moreover, the obtained LSV curves of S-Bi_2O_3 and Ce@S-Bi_2O_3 electrocatalysts show a higher current density and positive onset potential than Bi_2O_3. Significantly, the Ce@S-Bi_2O_3 electrocatalyst was outperformed with more onset potential (−1.16 V vs RHE) and higher current density in wide potential ranges compared to other investigated electrocatalysts.[17, 62, 63] Notably, for instance, Ce@S-Bi_2O_3 showed a current density of 42.07 and 6.01 mA cm^{-2} at −1.16 V versus RHE in CO_2 and N_2-saturated electrolyte, respectively, a difference of 6.8 times higher compared to N_2-saturated conditions (Figure 3b). To clarify the performance of ECO_2RR, chronoamperometry (CA) curves (i–t) were obtained across various potentials ranging from −0.76 to −1.26 V versus RHE as shown in Figure 3c. Furthermore, the ECO_2RR intrinsic activity of Bi_2O_3 and S-Bi_2O_3 electrocatalysts was analyzed by a CA technique for 2 h at different applied potentials. The produced liquid product formate was identified using proton nuclear magnetic resonance spectroscopy (^{1}H-NMR), as shown in Figure S11 (Supporting Information). Figure 3d shows the FE of formate for Bi_2O_3, S-Bi_2O_3, and Ce@S-Bi_2O_3 electrocatalysts. In that, the Ce@S-Bi_2O_3 electrocatalyst achieved $FE_{formate}$ over 92.5% at −1.16 V versus RHE, and it has a much higher formate selectivity compared to the Bi_2O_3 and S-Bi_2O_3, which had $FE_{formate}$ values of 80% and 83%, respectively, at the same potentials. Among all three examined electrocatalysts, the Ce@S-Bi_2O_3 hierarchical nanosheets exhibited higher current density (49.9 mA cm^{-2}) compared to Bi_2O_3 (25.3 mA cm^{-2}) and S-Bi_2O_3 (27.02 mA cm^{-2}) at −1.16 V versus RHE, as shown in Figure 3e. Also, the achieved higher $FE_{formate}$ and $j_{formate}$ of Ce@S-Bi_2O_3 electrocatalyst is comparable to the recently reported Bi-based electrocatalysts in an H-cell (Table S6, Supporting Information). In addition, electrocatalysts display much higher formate partial current densities

($j_{formate}$) in the different potentials during CA analysis, as shown in Figure S12a,b (Supporting Information).

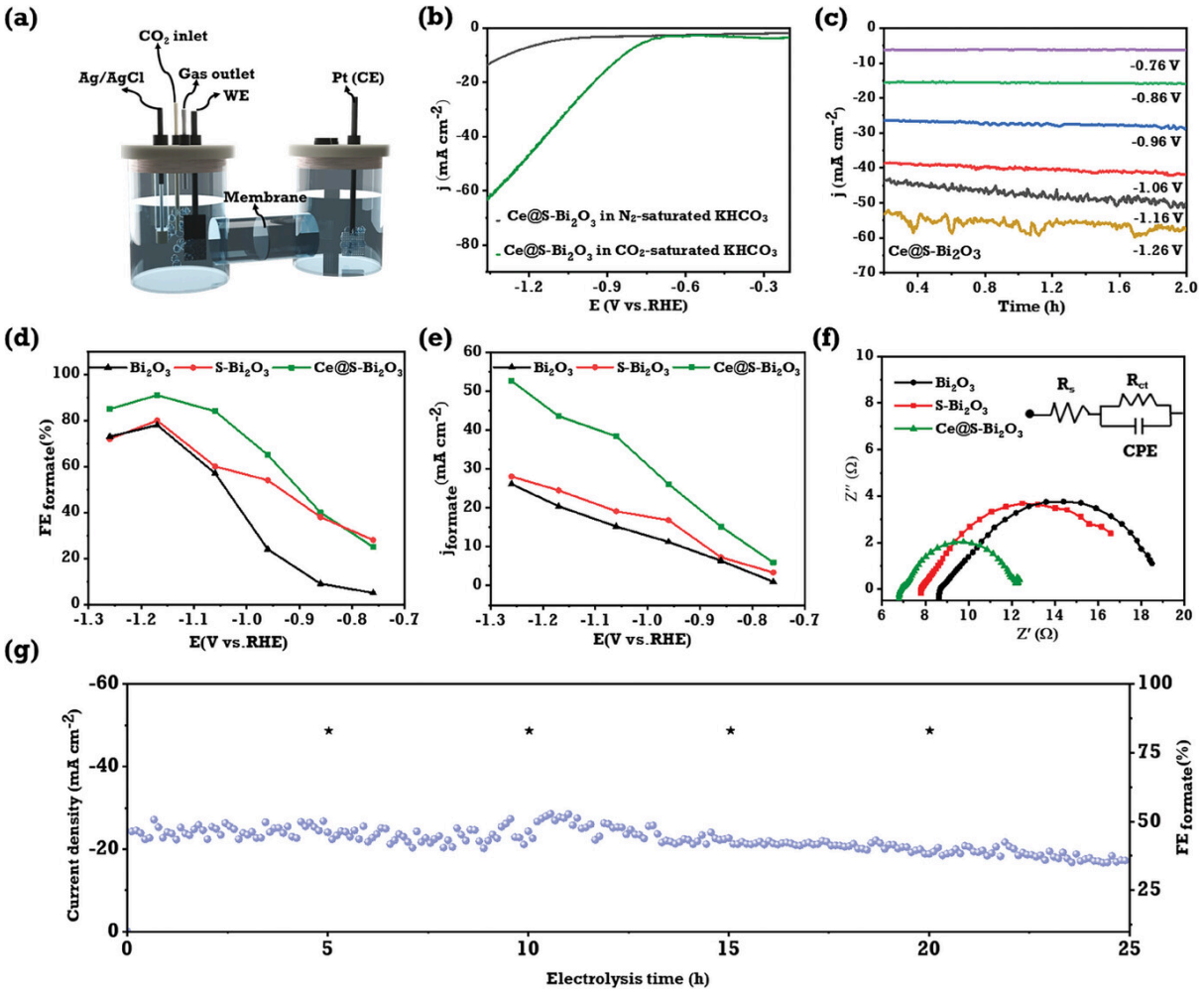

Figure 3

ECO_2RR performance of Ce@S-Bi_2O_3 electrocatalyst. a) Schematic diagram of H-cell. b) LSV curve of Ce@S-Bi_2O_3 electrocatalyst under N_2 and CO_2 saturated 0.5 M $KHCO_3$ electrolyte with a scan rate of 5 mV s^{-1}. c) Chronoamperometry measurements of Ce@S-Bi_2O_3 electrocatalyst at different applied potentials (from −0.76 to −1.26 V vs RHE) for electrochemical CO_2RR. d) $FE_{formate}$ of Ce@S-Bi_2O_3 electrocatalyst. e) The partial current density of formate ($j_{formate}$) for Bi_2O_3, S-Bi_2O_3, and Ce@S-Bi_2O_3 electrocatalysts. f) Electrochemical impedance Spectra of ECO_2RR at the corresponding electrocatalyst, insert are equivalent circuits used for fitting, and g) Stability tests of Ce@S-Bi_2O_3 electrocatalysts at -0.96 V versus RHE in 0.5 M $KHCO_3$ electrolyte.

In addition, the Tafel slope (log (j mA cm^{-2}) vs overpotential) as shown in Figure S13a–c (Supporting Information) the Ce@S-Bi_2O_3 (257 mv dec^{-1}) has a lower Tafel slope compared to Bi_2O_3 (286 mv dec^{-1}) and S-Bi_2O_3 (273 mv dec^{-1}), which confirmed the improved reaction kinetics of the Ce@S-Bi_2O_3 electrocatalyst over the other un-doped electrocatalysts in ECO_2RR.[64] Also, the electrochemical active surface area was estimated from the double-layer capacitance (C_{dl}) to understand the activity of the prepared electrocatalyst during ECO_2RR. The results in

Figure S14a–d (Supporting Information) show the C_{dl} values of Bi_2O_3, S-Bi_2O_3, and Ce@S-Bi_2O_3 (0.94, 0.87, and 1.12 mF cm^{-2}, respectively). ECSA was calculated from the C_{dl} values, and the results show that Ce@S-Bi_2O_3 exhibits a relatively higher active surface area of 28.0 cm^{-2} compared to Bi_2O_3 (23.5 cm^{-2}) and S-Bi_2O_3 (21.7 cm^{-2}). This indicates that the highly efficient active surface area sites and mass transfer of Ce@S-Bi_2O_3 are more suitable for ECO_2RR.[65] Furthermore, the turn over frequency (TOF) was calculated for Bi_2O_3 (0.0234 S^{-1}), S-Bi_2O_3 (0.0296 S^{-1}), and Ce@S- Bi_2O_3 (0.05624 S^{-1}) at the corresponding current potential (−1.16 V vs RHE). These results further indicate that the Ce@S-Bi_2O_3 hierarchical nanosheets are favorable for creating more abundant active sites on the electrocatalyst surface for improving the ECO_2RR activity. Electrochemical impedance spectroscopy (EIS) was carried out to investigate the electron kinetics charge transfer resistance as shown in Figure 3f. The charge transfer resistance (R_{ct}) of Ce@S-Bi_2O_3 (3.3 Ω) shows better conductivity than that of S-Bi_2O_3 (3.6 Ω) and Bi_2O_3 (4.2 Ω) electrocatalysts, as demonstrated in the Nyquist plots. The corresponding fitted data using the equivalent circuit diagram are shown in insert Figure 3f. The lower R_{ct} values indicate better electronic conductivity and charge transfer process of the Ce@S-Bi_2O_3 electrocatalyst. These specific findings showed that the hierarchical nanosheets facilitate faster charge carrier migration to the Ce@S-Bi_2O_3 electrocatalyst surface.[66–68] To evaluate the stability of the hierarchical nanosheet Ce@S-Bi_2O_3 electrode, CA analysis was performed at −0.96 V versus RHE for >25 h. The current density was stable at ≈21 mA cm^{-2}, and the FE of formate remained unchanged (86% ± 2%) during CA analysis, as demonstrated in Figure 3g. The S has lower electronegativity than oxygen (O), thus reducing the Bi oxidation state in S-Bi_2O_3 electrocatalyst. The lower amount of S-doping enhanced the catalytic activity by modifying the surface electronic structure Bi-metal sites. Also, the S-doping decreased the energy barrier of intermediate and obstructed the adsorption *H, which suppressed the evaluation of H_2.[69,46] Moreover, doping of S with Ce in Bi_2O_3 further enhanced the formate selectivity due to its better intrinsic activity. Specifically, the Ce doping created more numerous active Bi sites and facilitated the dissociation of H_2O to form absorbed H* intermediate, eventually enhancing $FE_{formate}$ during ECO_2RR.[31,45] In addition, role of Ce and S- doping in Bi_2O_3 was theoretically investigated and discussed in DFT section.

2.3 Post Electrochemical Analysis

Additionally, FE-SEM and HR-TEM analyses were carried out after 2 h of the ECO_2RR to understand the structural and electrochemical stability of the Ce@S-Bi_2O_3 electrocatalyst. The results in Figures S15 and S16 (Supporting Information) show the appreciable surface structure and intensity of the elements in EDX analysis. HR-TEM images in Figure S15a,b (Supporting Information) show the retention of catalyst elements distributed uniformly without agglomeration. After ECO_2RR the electrocatalyst exhibits the d-spacing value of Bi (0.323 nm) corresponds to the (012) plane well match with metallic Bi^0, which indicate the conversion of Bi^{3+} to metallic Bi^0.[10] Also, the SAED pattern in Figure S16c (Supporting Information) illustrates the improved crystallinity nature of Ce@S-Bi_2O_3 electrocatalyst. The EDS mapping in Figure S16d,e (Supporting Information) confirmed the uniform distribution of elements in the hierarchical nanosheets. Respective elemental maps confirmed the presence of Ce, S, and O elements with decreases in their respective concentration. Figure S16f (Supporting Information) shows the corresponding EDS spectrum with an appreciable intensity of all the elements and the metal composition in the selected mapping area. To understand the structural state of catalysts during the ECO_2RR process, we have performed time-dependent XRD analysis and shown in Figure S17a (Supporting Information). The analysis is performed under different reaction time at an applied potential of −1.16 V versus RHE. For the Ce@S-Bi_2O_3 electrode, with the increasing reaction time of ECO_2RR (from 120 s), the diffraction peaks of Bi_2O_3 (JCPDS#27-

0052) reduce gradually. Furthermore, the diffraction peaks of Bi (JCPDS#85-1330) and $Bi_2O_2CO_3$ (JCPDS#41-1488) appear completely after 2 h.[70,71] Furthermore XPS analysis performed after ECO_2RR and shown in Figure S17b (Supporting Information) to understand the elements state and chemical composition of the catalyst. In that, the Bi $4f_{7/2}$ and Bi $4f_{5/2}$ peaks initially at 159.2 and 164.5 eV were shifted to 158.1 and 163.3 eV (Bi $4f_{7/2}$ = 1.11 eV and Bi $4f_{5/2}$ = 1.12 eV), which agree with the obtained d-spacing values from the HR-TEM results. The reduced Bi^{3+} electrons are more beneficial for CO_2 to formate conversion than their initial nature.[72,73,8] After ECO_2RR Figure S17c (Supporting Information) revealed that the peak located at 530.2 eV in the O1s spectrum belongs to the Bi─O (O_{lat}), and the adsorbed oxygen peak (O_{ads}) is located at 532.8 eV. After electrochemical CO_2 reduction, the O-vacancy sites were entirely reduced to metallic Bi species.[74,10] Furthermore, Figure S17d and Table S2 (Supporting Information) revealed that, in Ce 3d, the valence state of Ce^{4+} ions gradually reduced to Ce^{3+} ions, which are more favorable for formate selectivity during the ECO_2RR. As shown in Table S2 (Supporting Information), we have performed ICP-OES analysis for Ce@S-Bi_2O_3 electrocatalyst before and after ECO_2RR to study the changes in the composition of Bi, Ce, and S. The electrocatalyst after ECO_2RR showed a nominal decrease in the concentrations of Bi, Ce and S compared to fresh electrocatalyst. This decrease in the concentrations may be due to the leaching during a prolonged stability test.[46] However, this does not affect the current density and selectivity of electrocatalytst throughout the stability test as evidenced from Figure 3g. Finally, the post ECO_2RR investigations revealed that the optimized Ce@S-Bi_2O_3 electrocatalyst displays structural retention and formation of a promising chemical nature.

2.4 Electrochemical CO_2 Reduction in GDE Reactor

Evaluating ECO_2RR Ce@S-Bi_2O_3 electrocatalysts in three-chamber GDE reactors is an effective way to screen electrocatalysts, understand structure-performance relationships, and gain mechanistic insights, as in Figure 4a.[75] The Ce@S-Bi_2O_3 represents a more positive onset potential and increases the current density compared to Bi_2O_3 and S-Bi_2O_3, suggesting it is a suitable catalyst for ECO_2RR. The obtained electrochemical reduction products corresponding to different applied potentials (−0.76 to −1.36 eV vs RHE) were measured using online gas chromatography and ion chromatography. The much higher $FE_{formate}$ was obtained for Ce@S-Bi_2O_3 than for S-Bi_2O_3 and Bi_2O_3 electrocatalyst in the analyzed potential region from −0.76 to −1.36 eV versus RHE. Notably, the highest $FE_{formate}$ (88.9%) was obtained at −1.06 eV versus RHE (40.90 mA cm^{-2}) in the Ce@S-Bi_2O_3 electrocatalyst. As shown in Figure 4d, formate is the dominant product from the electrochemical CO_2 reduction using Ce@S-Bi_2O_3 electrocatalyst. CO and H_2 gases were also detected as minority products in ECO_2RR. The Ce@S-Bi_2O_3 electrocatalyst demonstrated high FE (> 80%) toward formate in a wide potential window (of −0.76 to −1.36 eV) versus RHE. At a lower cathodic potential of −0.76 eV, significant H_2 evolution takes place with a corresponding FE of 32.4%. Upon obtaining the potential, the H_2 evolution is suppressed, and CO contribution starts to increase and reaches a maximum FE_{CO} of 13% at −1.16 eV. Notably, the S containing S-doped Bi_2O_3 and Ce@S-Bi_2O_3 electrocatalysts enhanced the dissociation of H_2O and increase the H^+, which might react with CO_2 to form OCHO*,suppresses H_2 formation and promotes formate selectivity at low overpotentials (−0.76 to −1.36 eV vs RHE) in ECO_2RR.[76] Also compared to single metal Bi-S-O catalysts Ce doped Ce-Bi-S-O catalyst exhibit more superior catalytic performance in the formate selectivity, it is clearly confirm from the obtained results shown in Figure 4d. At a higher potential of −1.36 eV, H_2 starts to rise again. The reason for enhanced H_2 evolution and at

a higher potential is the mass transport limitation of CO_2 to the electrode at higher currents. The current densities also increased with an increase in the potential. Although the FE at −1.36 V was slightly lower than at −1.26 V (due to the higher current at −1.36 V), the partial current density of formate is higher (54.13 mA cm^{-2}) than the 49.93 mA cm^{-2} for −1.26 V versus RHE under a CO_2 atmosphere increase in order, this results from the enhanced conductivity of the Ce@S-Bi_2O_3 catalyst shown in Figure 4d. In addition, gas phase products were measured through an online gas chromatogram, and no gas products other than CO and H_2 were observed on gas chromatography. The presence of formate is identified from the ion chromatogram from the Ce@S-Bi_2O_3 electrocatalyst. The products for S-Bi_2O_3 and Bi_2O_3 catalysts were also determined at −1.36 eV versus RHE. The $FE_{formate}$ were slightly lower, with values of 83 and 81%, respectively. The partial current density toward formate for Bi_2O_3 was 41.4 mA cm^{-2} and that for S-Bi_2O_3 was 43.0 mA cm^{-2}, which is much lower than that toward Ce@S-Bi_2O_3, as shown in Figure 4b,c. Through these experiments, it was determined that Ce@S-Bi_2O_3 is the best catalyst in the sequence for selective formate production by ECO_2RR. Notably, Ce@S-Bi_2O_3 electrocatalyst delivers a higher partial current density for formate than Bi_2O_3 and S-Bi_2O_3. Ce doped at the S- Bi_2O_3 provides a high formate current density in ECO_2RR. Moreover, all the investigated catalysts (Bi_2O_3, S-Bi_2O_3, and Ce@S-Bi_2O_3) showed the highest $j_{formate}$ achieved at −1.06 eV versus RHE. Furthermore, the stability of the Ce@S-Bi_2O_3 electrocatalyst was evaluated in a GDE flow reactor at an applied potential of −1.2 V versus RHE, for a continuous reaction of up to 5 h. Figure S18b (Supporting Information) shows that there is no significant change in the current density during the stability analysis. The FE of formate is also sustained at over 72% for up to 4 h of reaction shown in Figure S18a (Supporting Information). However, after 4 h, the FE of formate decreased to 65% and H_2 FE increased to 28%, which could be due to the flooding of GDE.[77] A similar phenomenon was observed in our previous study as well.[78]

2.5 Theoretical Calculations

We conducted calculations to determine the optimal adsorption structures and energetics of *CO_2, *COOH, *OCHO, *CO, and *HCOOH species for the purpose of electrochemical CO_2 RR. These calculations were performed on the (111) plane of Bi_2O_3, S-Bi_2O_3, and Ce@S-Bi_2O_3, as shown in Figures S19 and S22 (Supporting Information). The Gibbs free energy (ΔG) associated with the creation of *COOH, which serves as an intermediary in the CO pathway, is greater than that of *OCHO, which serves as an intermediate in the HCOOH pathway in pure Bi_2O_3 as depicted in Figure 5a. Additionally, the introduction of S-doping on the surface of Bi_2O_3 effectively reduced the reaction route for the *OCHO intermediate, as illustrated in Figure 5b. On S-doped Bi sites, the Gibbs free energies (ΔG) for creating *OCHO and *HCOOH through the HCOOH pathway were 0.63 and 0.14 eV, respectively.

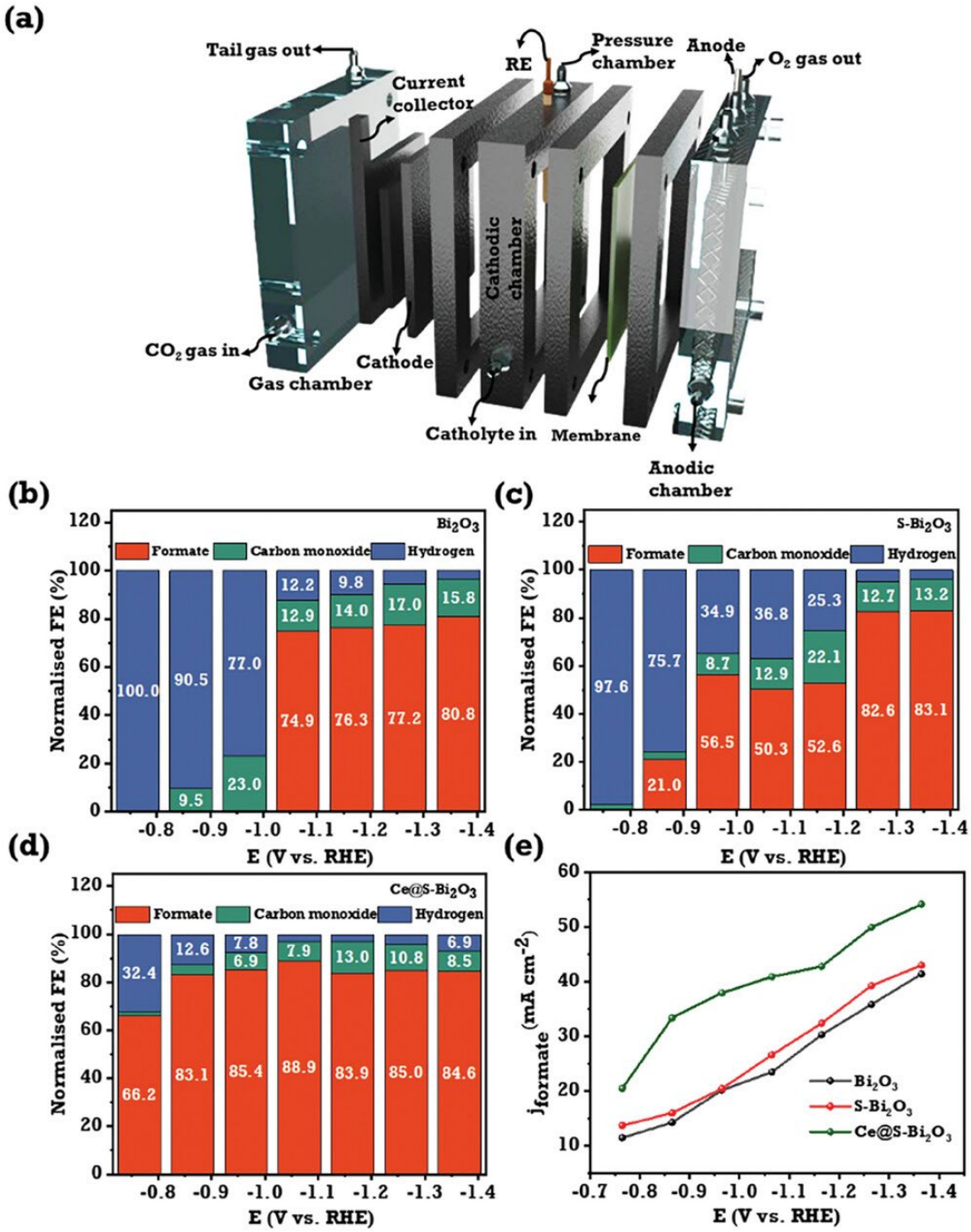

Figure 4

The Ce@S-Bi_2O_3 electrocatalyst performance and testing in three-chamber GDE reactor. a) Schematic illustration of GDE reactor cell used for the experiment. b–d) FE of products (formate, CO, and H_2) distributions at different potentials applied on Bi_2O_3, S-Bi_2O_3, and Ce@S-Bi_2O_3 hierarchal nanosheet. e) The formate partial current density ($j_{formate}$) for Bi_2O_3, S-Bi_2O_3, and Ce@S-Bi_2O_3 electrocatalyst at corresponding potentials in the CO_2- saturated 0.5 M $KHCO_3$ electrolyte media.

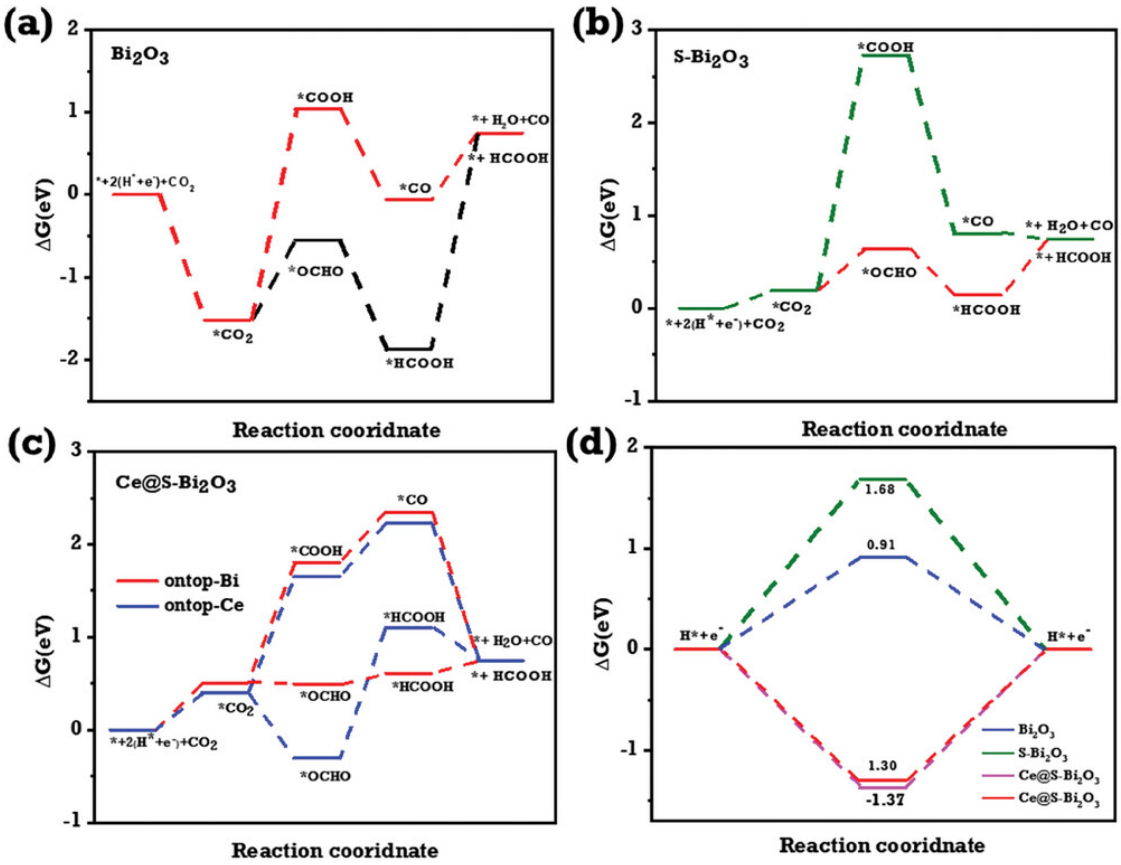

Figure 5

a) Gibbs free energy diagrams for electrochemical CO_2RR to *CO and *HCOOH on Bi_2O_3 (111), and b) S-Bi_2O_3 (111) surface. c) Gibbs free energy diagrams for ECO_2RR to various intermediates form on the surface of Bi (111) and Ce sites, and d) Gibbs free energy diagrams for H_2 on the surface of Bi_2O_3, S-Bi_2O_3, and Ce@S-Bi_2O_3 on top of Bi and Ce.

The introduction of S on Bi significantly reduced the Gibbs free energy for both. Furthermore, Ce and S were doped onto Bi_2O_3, suggesting that the *OCHO pathway is more energetically favorable than the CO pathway, as shown in Figure 5c and Tables S3 and S4 (Supporting Information). The electrocatalyst of Ce@S-Bi_2O_3 was established to facilitate the conversion of CO_2 to *OCHO efficiently and readily with no barrier in the case of Ce@S-Bi_2O_3 electrocatalyst. We also performed several models of Ce and S-doped Bi_2O_3, as shown in Figure S23 and Table S5 (Supporting Information). This consistently demonstrates that the reactions involving formate (*OCHO) are endothermic, suggesting that the rate-determining step (RDS) for formate is favorable when Bi_2O_3 is doped with Ce and S.

Furthermore, the Gibbs free energy diagram illustrating the process of hydrogen evolution reaction (HER) on the surfaces of Bi_2O_3, S-Bi_2O_3, and Ce@S-Bi_2O_3 is depicted in Figure 5d. The lower formation of H* species means a higher activity of H_2O dissociation on the electrocatalytic surface.[31,79] Energy barriers associated with HER on Ce@S-Bi_2O_3 are more significant compared to those on Bi_2O_3 and S-Bi_2O_3 surfaces. This indicates a significant inhibition of HER following the introduction of Ce and S-doping in Bi_2O_3.These calculated parameters are well agreement with experimental ECO_2RR results of S and Ce modified Bi_2O_3

electrocatalyst (Figure 3d). In addition, the disparity in limiting potentials between the ECO_2RR and HER, denoted as UL(CO_2RR)-UL(H_2), was computed. This parameter has been established as a crucial indicator of ECO_2RR selectivity, with a more significant positive UL(CO_2)-UL(H_2) value corresponding to more considerable selectivity as shown in Figure S24 (Supporting Information). As anticipated, the Ce@S-Bi_2O_3 results in a higher positive UL (CO_2RR)-UL(H_2) compared to both S-doped Bi_2O_3 and pure Bi_2O_3 electrocatalysts,[38,80] Experimental and computational results indicate that this is an impressive ECO_2RR for the Ce@S-Bi_2O_3 electrocatalyst. Considering all the parameters, the Ce@S-Bi_2O_3 group has a significant role in determining the free energy of reaction intermediates and CO_2 reduction activity.

3 Conclusion

In summary, we developed efficient Ce@S-Bi_2O_3 hierarchical nanosheets for ECO_2RR for formate production. The obtained structural and morphological results confirmed the formation of crystalline hierarchical nanosheets. Notably, the BET results confirmed the formation of large-surface area Bi_2O_3 (50.48 $m^2\ g^{-1}$) during S modification. The Ce and S-doped Bi_2O_3 electrocatalyst showed improved electrocatalytic activity and long-term durability with $FE_{formate}$ of 90% in a wide potential window of both fabricated H-cell and GDE reactor. The obtained XPS results confirmed that the S and Ce doping induced a modification in the Bi site electronic configuration that facilitated CO_2 adsorption and improved electron transfer to produce a high conversion rate of formate. Moreover, DFT calculations confirmed that Ce and S optimized the adsorption of *CO and *OCHO intermediates in the ECO_2RR. Including Ce in the S-Bi_2O_3, the electrocatalyst minimizes the energy barrier of intermediates on the Bi sites. Therefore, this study provides a new strategy in the development of highly efficient electrocatalysts for formate production by ECO_2RR.

4 Experimental Section

Materials

Bismuth nitrate pentahydrate (Bi $(NO_3)_2{\cdot}5H_2O$, 99.99%), cerium nitrate hexahydrate (Ce $(NO_3)_2{\cdot}6H_2O$, 99.99%), thioacetamide (TAA,98%), ethylene glycol (EG, 99.98%), potassium bicarbonate ($KHCO_3$, 99.7%), and Nafion solution (5 wt.%) were purchased from Sigma–Aldrich. Hydrochloric acid (HCl, 37%), sulfuric acid (H_2SO_4, 98%), and hydrogen peroxide (H_2O_2, 35%) were obtained from Daejung Chemicals and Metals. Ethanol (EtOH, 99.5%) and acetone (99.5%) were purchased from Samchun Pure Chemical Co. Ltd. and Duksan Reagents (South Korea), respectively.

Synthesis of Bi_2O_3 and S-Bi_2O_3

First, bismuth nitrate pentahydrate Bi $(NO_3)_2{\cdot}5H_2O$ (50 mM) and thioacetamide (3 mM) were dissolved in EtOH and EG (2:1% volume) aqueous solution. The mixed solution was stirred for 30 min, transferred to a 50 mL polytetrafluoroethylene (PTFE)-lined stainless-steel autoclave, and heated at 170°C for 6 h. After hydrothermal treatment, the precipitate was collected, centrifuged, and washed with deionized water and EtOH. The obtained product was dried in a vacuum oven at 70˚C overnight. The

final product was labeled as S-Bi_2O_3. The Bi_2O_3 was prepared similarly except for adding thioacetamide (C_2H_5NS).

Synthesis of Ce@S-Bi_2O_3

The preparation of Ce@ S-Bi_2O_3 hierarchical nanosheets first involved adding Bi $(NO_3)_2 \cdot 5H_2O$ (45 mM) and Ce $(NO_3)_2 \cdot 6H_2O$ (5 mM) into a solution containing EtOH and EG (2:1%volume). After vigorous stirring for 30 min, the solution was transferred to a 70 mL stainless steel PTFE autoclave and heated at 170 °C (heating rate 5 °C min^{-1}) for 6 h in an air atmosphere. The products were collected and centrifuged with deionized water and EtOH several times. The obtained powder was dried in a vacuum overnight. The Ce@S-Bi_2O_3 hierarchical nanosheets were successfully prepared. During the synthesis, Ce and S ratios were optimized to obtain the highest electrocatalytic activity in terms of ECO_2RR to formate conversions. The ratios of the highest FE were reported in the synthesis protocols.

Electrochemical Analysis from an H-Cell

An ECO_2RR was performed using an electrochemical H-cell separated by a proton exchange membrane (Nafion-212). The reference electrode (Ag/AgCl) and working electrode were placed in the cathode compartment, and the counter electrode (Pt-mesh) was placed in the anode compartment. A 0.5 M $KHCO_3$ solution (pH 7.4) in electrolyte was used as a catholyte throughout the reaction. Before performing the ECO_2RR, the cathode compartment was saturated with CO_2 (gas) (99.99% purity, BOC) by purging at 0.04 MPa (40 mL min^{-1}) for 30 min throughout the electrolysis. All potentials measured against the reference electrode were converted to the RHE scale using E (vs RHE) = E (vs. Ag/AgCl) + 0.197 V + 0.0591xpH. The ECO_2RR activity was investigated using CA and LSV at a scan rate of 5 mV s^{-1} at standard temperature and pressure.

Electrochemical CO_2RR Test in a GDE Reactor

Quantification of the products for various electrocatalysts was performed in a three-chamber GDE reactor in a three-electrode mode described in the previous study.[78] The current set-up consists of GDE as the working electrode, Pt nanoparticle-coated Ti mesh as a counter electrode, and Ag/AgCl (3 M NaCl) as the reference electrode. In addition, 0.5 M $KHCO_3$ was utilized as an electrolyte in both electrode chambers. The electrolyte chambers were separated by a cation exchange membrane (Sustainion X37-50, Dioxide Materials) to stop cross-over of the liquid products. For the usual measurements, the reactor was operated in a batch mode. Pure CO_2 gas (99.99% purity, BOC) flow was kept at 20 mL min^{-1} and was controlled by a digital mass flow controller. The current densities were determined by dividing the current obtained by the GDE area by 2 cm^2.

Calculation of Faradic Efficiency in a GDE Reactor

The ECO_2RR products were analyzed by GC techniques. Gas products were measured by online GC using a Shin Carbon Micropacked column (Shimadzu Nexis GC-2030), where the outlet of the gas chamber was directly connected to the injection port of the GC, and samples

were collected at regular intervals. After ECO_2RR liquid products were analyzed, they were manually collected. Alcohols were analyzed using the above GC using a DB-wax column, and formate was analyzed using ion chromatography (Eco IC, Metrohm).[78]

FE refers to the ratio of current used to produce a particular product, expressed by Equation (1):

$$FE = \frac{znF}{Q} \quad (1)$$

Where z is the number of electrons required per mole of product, and n is the number of moles of product formed. F is Faraday's constant (96485 C mol^{-1}), and Q is the total charge passed through to the experiments. The total FE of the samples ranged from 80% to 91.5%. Gaseous products can affect the overall FE value, including side reactions of the catalytic reduction during the CO_2 reduction process, crossing of products through the GDE and the membrane, and averaging of the obtained currents. Total FE was normalized by 100% to allow direct comparison between the catalysts. The total voltage measured was highest in formate observed at −1.06 V at 41 mA cm^{-2}, and the highest current density of 54 mA cm^{-2} was observed at −1.36 V versus RHE for the Ce@S- Bi_2O_3 electrocatalyst.

Acknowledgements

This research work was supported by BK21 FOUR Program by Jeonbuk National University Research Grant. This research was supported by "Regional Innovation Strategy (RIS)" through the National Research Foundation of Korea (NRF) funded by the Ministry of Education (MOE) (2023RIS-008). This research was supported by Basic Science Research Program through the National Research Foundation of Korea (NRF) funded by the Ministry of Science, ICT and Future Planning (NRF-2020R1A2B5B01001458). The authors acknowledge the Korea Institute of Science and Technology Information (KISTI) for the computational resources provided for this research. This research work was partially supported by UKRI Circular Chemical Economy Centre (EP/V011863/1).

Conflict of Interest

The authors declare no conflict of interest.

1. J. Ni, Q. Cheng, S. Liu, M. Wang, Y. He, T. Qian, C. Yan, J. Lu, *Adv. Funct. Mater.* 2023, **33**, 2212483.
2. H. Liu, Y. Zhu, J. Ma, Z. Zhang, W. Hu, *Adv. Funct. Mater.* 2020, **30**, 1910534.
3. Álvarez, A. Bansode, A. Urakawa, A. V. Bavykina, T. A. Wezendonk, M. Makkee, J. Gascon, F. Kapteijn, *Chem. Rev.* 2017, **117**, 9804.
4. H. Shen, Y. Zhao, L. Zhang, Y. He, S. Yang, T. Wang, Y. Cao, Y. Guo, Q. Zhang, H. Zhang, *Adv. Energy Mater.* 2023, **13**, 2202818.
5. a) D. Wu, G. Huo, W. Y. Chen, X. Z. Fu, J. L. Luo, *Appl. Catal., B* 2020, **271**, 118957. b) M. Prasanna, N. Logeshwaran, S. Ramakrishnan, D. J. Yoo, *Small* 2023, **20**, 2306165.
6. Y. Hori, H. Wakebe, T. Tsukamoto, O. Koga, *Electrochim. Acta* 1994, **39**, 1833.
7. X. Zhang, Y. Zhang, Q. Li, X. Zhou, Q. Li, J. Yi, Y. Liu, J. Zhang, *J. Mater. Chem. A* 2020, **8**, 9776.

8. P. Deng, F. Yang, Z. Wang, S. Chen, Y. Zhou, S. Zaman, B. Y. Xia, *Angew. Chem., Int. Ed.* 2020, **59**, 10807.
9. Z. Wang, C. Wang, Y. Hu, S. Yang, J. Yang, W. Chen, H. Zhou, F. Zhou, L. Wang, J. Du, Y. Li, Y. Wu, *Nano Res.* 2021, **14**, 2790.
10. S. Liu, X. F. Lu, J. Xiao, X. Wang, X. W. Lou, *Angew. Chem., Int. Ed.* 2019, **58**, 13828.
11. J. Fan, X. Zhao, X. Mao, J. Xu, N. Han, H. Yang, B. Pan, Y. Li, L. Wang, Y. Li, *Adv. Mater.* 2021, **33**, 2100910.
12. Z. Wang, G. Yang, Z. Zhang, M. Jin, Y. Yin, *ACS Nano* 2016, **10**, 4559.
13. T. Montini, M. Melchionna, M. Monai, P. Fornasiero, *Chem. Rev.* 2016, **116**, 5987.
14. Y. Shi, Y. Zhou, D. R. Yang, W. X. Xu, C. Wang, F. B. Wang, J. J. Xu, X. H. Xia, H. Y. Chen, *J. Am. Chem. Soc.* 2017, **139**, 15479.
15. D. Tan, W. Lee, K. T. Park, Y. E. Jeon, J. Hong, Y. N. Ko, Y. E. Kim, *Appl. Surf. Sci.* 2023, **613**, 155944.
16. G. Wang, F. Wang, P. Deng, J. Li, C. Wang, Y. Hua, Y. Shen, X. Tian, *Mater. Rep.: Energy* 2023, **3**, 100181.
17. P. Lamagni, M. Miola, J. Catalano, M. S. Hvid, M. A. H. Mamakhel, M. Christensen, M. R. Madsen, H. S. Jeppesen, X. M. Hu, K. Daasbjerg, T. Skrydstrup, N. Lock, *Adv. Funct. Mater.* 2020, **30**, 1910408.
18. X. Wang, X. Sang, C. L. Dong, S. Yao, L. Shuai, J. Lu, B. Yang, Z. Li, L. Lei, M. Qiu, L. Dai, Y. Hou, *Angew. Chem., Int. Ed.* 2021, **60**, 11959.
19. P. Chen, T. Zhou, M. Chen, Y. Tong, N. Zhang, X. Peng, W. Chu, X. Wu, C. Wu, Y. Xie, *ACS Catal.* 2017, **7**, 7405.
20. K. Xu, H. Cheng, H. Lv, J. Wang, L. Liu, S. Liu, X. Wu, W. Chu, C. Wu, Y. Xie, *Adv. Mater.* 2018, **30**, 1703322.
21. J. Wang, S. Ning, M. Luo, D. Xiang, W. Chen, X. Kang, Z. Jiang, S. Chen, *Appl. Catal., B* 2021, **288**, 119979.
22. S. Ramakrishnan, J. Balamurugan, M. Vinothkannan, A. R. Kim, S. Sengodan, D. J. Yoo, *Appl. Catal., B* 2020, **279**, 119381.
23. T. TranPhu, R. Daiyan, Z. Fusco, Z. Ma, R. Amal, A. Tricoli, *Adv. Funct. Mater.* 2020, **30**, 1906478.
24. G. Wen, D. U. Lee, B. Ren, F. M. Hassan, G. Jiang, Z. P. Cano, J. Gostick, E. Croiset, Z. Bai, L. Yang, Z. Chen, *Adv. Energy Mater.* 2018, **8**, 1802427.
25. H. Wei, A. Tan, Z. Xiang, J. Zhang, J. Piao, Z. Liang, K. Wan, Z. Fu, *ChemSusChem* 2022, **15**, 202200752.
26. G. Zhang, X. Zheng, X. Cui, J. Wang, J. Liu, J. Chen, Q. Xu, *ACS Appl. Nano Mater.* 2022, **5**, 15465.
27. A.Zhang, Y. Liang, H. Li, X. Zhao, Y. Chen, B. Zhang, W. Zhu, J. Zeng, *Nano Lett.* 2019, **19**, 6547.
28. X. Li, N. Qian, L. Ji, X. Wu, J. Li, J. Huang, Y. Yan, D. Yang, H. Zhang, *Nanoscale Adv.* 2022, **4**, 2288.
29. J. Yan, Y. Guan, B. Marchetti, Y. Liu, F. Ning, J. Yi, X. D. Zhou, *Chem. Eng. J.* 2023, **467**, 143531.
30. J. H. Zhou, K. Yuan, L. Zhou, Y. Guo, M. Y. Luo, X. Y. Guo, Q. Y. Meng, Y. W. Zhang, *Angew. Chem., Int. Ed.* 2019, **58**, 14197.
31. W. Ma, S. Xie, X. G. Zhang, F. Sun, J. Kang, Z. Jiang, Q. Zhang, D. Y. Wu, Y. Wang, *Nat. Commun.* 2019, **10**, 892.

32. a) P. Li, F. Yang, J. Li, Q. Zhu, J. W. Xu, X. J. Loh, K. W. Huang, W. Hu, J. Lu, *Adv. Energy Mater.* 2023, **13**, 2301597. b) F. CalleVallejo, D. Loffreda, M. T. M. Koper, P. Sautet, *Nature Chemistry* 2015, **7**, 403.
33. A.Bagger, W. Ju, A. S. Varela, P. Strasser, J. Rossmeisl, *ChemPhysChem* 2017, **18**, 3266.
34. N. Han, Y. Wang, H. Yang, J. Deng, J. Wu, Y. Li, Y. Li, *Nat. Commun.* 2018, **9**, 1320.
35. Y. Mi, S. Zeng, L. Li, Q. Zhang, S. Wang, C. Liu, D. Sun, *Mater. Res. Bull.* 2012, **47**, 2623.
36. J. Bi, J. Che, L. Wu, M. Liu, *Mater. Res. Bull.* 2013, **48**, 2071.
37. Moorthy, M. R. Subramaniam, T. G. Manivasagam, D. Kumaresan, *Dalton Trans.* 2018, **47**, 8683.
38. S. Q. Liu, M. R. Gao, R. F. Feng, L. Gong, H. Zeng, J. L. Luo, *ACS Catalysis* 2021, **11**, 7604.
39. M. Zhang, W. Wei, S. Zhou, D. D. Ma, A. Cao, X. T. Wu, Q. L. Zhu, *Energy & Environm. Sci.* 2021, **14**, 4998.
40. D. Liu, X. Yan, P. Guo, Y. Yang, Y. He, J. Liu, J. Chen, H. Pan, R. Wu, *ACS Catalysis* 2023, **13**, 7698.
41. X. Cao, Y. Tian, J. Ma, W. Guo, W. Cai, J. Zhang, *Adv. Mater.* 2023, **36**, 2309648.
42. Q. Gong, P. Ding, M. Xu, X. Zhu, M. Wang, J. Deng, Q. Ma, N. Han, Y. Zhu, J. Lu, Z. Feng, Y. Li, W. Zhou, Y. Li, *Nat. Commun.* 2019, **10**, 2807.
43. a) L. Guo, F. Chen, X. Fan, W. Cai, J. Zhang, *Appl. Catal., B* 2010, **96**, 162; b) T. T. Le, V. C. Hoang, W. Zhang, J. M. Kim, J. Kim, G. Moon, S. H. Kim, *Chem. Eng. J. Adv.* 2022, **12**, 100371.
44. S. M. Yakout, *J. Environm. Chem. Eng.* 2020, **8**, 103644.
45. R. Yu, C. Qiu, Z. Lin, H. Liu, J. Gao, S. Li, Y. Yao, J. Yu, S. Yang, *ACS Mater. Lett.* 2022, **4**, 1749.
46. F. Liu, X. Ren, J. Zhao, H. Wu, J. Wang, X. Han, Y. Deng, W. Hu, *ACS Catalysis* 2022, **12**, 13533.
47. W. D. Chen, X. Q. Li, L. H. Duan, X. L. Xie, Y. D. Cui, *Appl. Surface Sci.* 1996, **100–101**, 592.
48. H. Li, G. Wang, F. Zhang, Y. Cai, Y. Wang, I. Djerdj, *RSC Adv.* 2012, **2**, 12413.
49. Y. X. Duan, Y. T. Zhou, Z. Yu, D. X. Liu, Z. Wen, J. M. Yan, Q. Jiang, *Angew. Chem., Int. Ed.* 2021, **60**, 8798.
50. R. S. Kumar, S. Prabhakaran, S. Ramakrishnan, S. C. Karthikeyan, A. R. Kim, D. H. Kim, D. J. Yoo, *Small* 2023, **19**, 2207096.
51. a) A. Hezam, K. Namratha, Q. A. Drmosh, D. Ponnamma, J. Wang, S. Prasad, M. Ahamed, C. Cheng, K. Byrappa, *ACS Appl. Nano Mater.* 2020, **3**, 138; b) D. Jiang, W. Wang, L. Zhang, Y. Zheng, Z. Wang, *ACS Catalysis* 2015, **5**, 4851.
52. P. H. Li, Z. Y. Song, M. Yang, S. H. Chen, X. Y. Xiao, W. Duan, L. N. Li, X. J. Huang, *Analyt. Chem.* 2020, **92**, 16089.
53. H. Shen, J. Bu, W. Wang, C. Wu, Y. Cao, B. Zhang, Q. Zhang, H. Zhang, *Chin. J. Chem.* 2020, **38**, 1353.
54. B. Cui, Y. Li, S. Li, Y. Xia, Z. Zheng, Y. Q. Liu, *Energy Fuels* 2020, **34**, 9932.
55. K. Masula, Y. Bhongiri, G. Raghav Rao, P. Vijay Kumar, S. Pola, M. Basude, *Opt. Mater.* 2022, **126**, 112201.
56. J. Henych, M. Št'astný, Z. Němečková, M. Kormunda, Z. Šanderová, Z. Žmudová, P. Ryšánek, Š. Stehlík, J. Ederer, M. Liegertová, J. Trögl, P. Janoš, *ACS Appl. Nano Mater.* 2022, **5**, 17956.
57. M. Prekajski, Z. Dohčević-Mitrović, M. Radović, B. Babić, J. Pantić, A. Kremenović, B. Matović, *J. Eur. Ceram. Soc.* 2012, **32**, 1983.

58. C. Silva, F. A. Sigoli, I. O. Mazali, *J. Phys. Chem. C* 2017, **121**, 12928.
59. J. Mei, T. Liao, G. A. Ayoko, Z. Sun, *ACS Appl. Mater. Interfaces* 2019, **11**, 28205.
60. S. Wu, M. Tian, Y. Hu, N. Zhang, W. Shen, J. Li, L. Guo, P. Da, P. Xi, C. H. Yan, *Inorganic Chemistry* 2023, **62**, 4088.
61. T. Tsujiguchi, Y. Kawabe, S. Jeong, T. Ohto, S. Kukunuri, H. Kuramochi, Y. Takahashi, T. Nishiuchi, H. Masuda, M. Wakisaka, K. Hu, G. Elumalai, J. Fujita, Y. Ito, *ACS Catalysis* 2021, **11**, 3310.
62. L. Fan, Z. Xia, M. Xu, Y. Lu, Z. Li, *Adv. Funct. Mater.* 2018, **28**, 1706289.
63. Z. Weng, X. Zhang, Y. Wu, S. Huo, J. Jiang, W. Liu, G. He, Y. Liang, H. Wang, *Angew. Chem., Int. Ed.* 2017, **56**, 13135.
64. R. Boppella, M. Austeria P, Y. Kim, E. Kim, I. Song, Y. Eom, D. P. Kumar, M. Balamurugan, E. Sim, D. H. Kim, T. K. Kim, *Adv. Funct. Mater.* 2022, **32**, 2202351.
65. S. Ramakrishnan, D. B. Velusamy, S. Sengodan, G. Nagaraju, D. H. Kim, A. R. Kim, D. J. Yoo, *Appl. Catal., B* 2022, **300**, 120752.
66. F. Yang, A. O. Elnabawy, R. Schimmenti, P. Song, J. Wang, Z. Peng, S. Yao, R. Deng, S. Song, Y. Lin, M. Mavrikakis, W. Xu, *Nat. Commun.* 2020, **11**, 1088.
67. D. Yao, C. Tang, A. Vasileff, X. Zhi, Y. Jiao, S. Z. Qiao, *Angew. Chem., Int. Ed.* 2021, **60**, 18178.
68. L. Lin, X. He, X. G. Zhang, W. Ma, B. Zhang, D. Wei, S. Xie, Q. Zhang, X. Yi, Y. Wang, *Angew. Chem., Int. Ed.* 2023, **62**, 202214959.
69. S. Liang, J. Xiao, T. Zhang, Y. Zheng, Q. Wang, B. Liu, *Angew. Chem., Int. Ed.* 2023, **62**, 202310740.
70. W. Ma, J. Bu, Z. Liu, C. Yan, Y. Yao, N. Chang, H. Zhang, T. Wang, J. Zhang, *Adv. Funct. Mater.* 2021, **31**, 2006704.
71. X. Ren, F. Liu, H. Wu, Q. Lu, J. Zhao, Y. Liu, J. Zhang, J. Mao, J. Wang, X. Han, Y. Deng, W. Hu, *Angew. Chem., Int. Ed.* 2024, **63**, 202316640.
72. a) X. Wang, W. Wang, B. Liu, Z. Song, Z. Ren, H. Fu, *Small* 2023, **19**, 2304084; b) Z. Gao, M. Hou, Y. Shi, L. Li, Q. Sun, S. Yang, Z. Jiang, W. Yang, Z. Zhang, W. Hu, *Chem. Sci.* 2023, **14**, 6860.
73. Y. Liu, Z. X. Lou, X. Wu, B. Mei, J. Chen, J. Y. Zhao, J. Li, H. Y. Yuan, M. Zhu, S. Dai, C. Sun, P. F. Liu, Z. Jiang, H. G. Yang, *Adv. Mater.* 2022, **34**, 2202568.
74. a) S. Ansari, M. S. Ansari, H. Devnani, S. P. Satsangee, R. Jain, *Sens. Actuat. B: Chem.* 2018, **273**, 1226. b) J. Wu, H. Xu, W. Yan, *Appl. Surface Sci.* 2016, **386**, 1.
75. H. Xiang, S. Rasul, K. Scott, J. Portoles, P. Cumpson, E. H. Yu, *J. CO2 Util.* 2019, **30**, 214.
76. F. Li, L. Chen, M. Xue, T. Williams, Y. Zhang, D. R. MacFarlane, J. Zhang, *Nano Energy* 2017, **31**, 270.
77. Y. Kong, H. Hu, M. Liu, Y. Hou, V. Kolivoška, S. Vesztergom, P. Broekmann, *J. Catal.* 2022, **408**, 1.
78. P. K. Sharma, S. Rasul, D. Li, E. H. Yu, *Materials Reports: Energy* 2023, **3**, 100196.
79. T. Shinagawa, G. O. Larrazábal, A. J. Martín, F. Krumeich, J. Pérez-Ramírez, *ACS Catalysis* 2018, **8**, 837.
80. H. Shang, T. Wang, J. Pei, Z. Jiang, D. Zhou, Y. Wang, H. Li, J. Dong, Z. Zhuang, W. Chen, *Angew. Chem., Int. Ed.* 2020, **59**, 22465.

Surface area-enhanced cerium and sulfur-modified hierarchical bismuth oxide nanosheets for electrochemical carbon dioxide reduction to formate

Naveenkumar Palanimuthu [a], Mohan Raj Subramaniam [a], Muthu Austeria P [b], Preetam Kumar Sharma [c,d], Vinoth Ramalingam [e], Karthik Peramaiah [f], Shanmugam Ramakrishnan [a,g], Geun Ho Gu [b], Eileen Hao Yu [d], and Dong Jin Yoo [a, h*]

[a] Graduate School, Department of Energy Storage/Conversion Engineering (BK21 FOUR), Hydrogen and Fuel Cell Research Center, Jeonbuk National University, Jeonju, Jeollabuk-do 54896, Republic of Korea

[b] Department of Energy Engineering, Korea Institute of Energy Technology (KENTECH), Naju, 58330, Republic of Korea

[c] Institute for Materials Discovery, University College London, Malet Place, London, WC1E 7JE, United Kingdom

[d] Department of Chemical Engineering, Loughborough University, Loughborough, LE11 3TU, United Kingdom

[e] School of Engineering, Robert Gordon University, Garthdee Road, Aberdeen AB10 7GJ, United Kingdom

[f] Agency for Science, Technology, and Research, Institute of Sustainability for Chemicals, Energy and Environment, 1 Pesek Road, Jurong Island, Singapore 627833, Singapore

[g] School of Engineering, Newcastle University, Merz Court, Newcastle upon Tyne, NE17RU, United Kingdom

[h] Department of Life Science, Jeonbuk National University, Jeollabuk-do 54896, Republic of Korea

*Corresponding Author Email ID: djyoo@jbnu.ac.kr (D.J. Yoo)

1 Material characterization

The morphological analysis of all prepared electrocatalysts was investigated by field emission scanning electron microscope with energy-dispersive X-ray spectroscopy (EDS) with SUPRA 40 VP; Carl Zeiss, Germany) and high-resolution transmission electron microscope (HR-TEM; JEM-ARM200F, JEOL). The X-ray diffraction (XRD) pattern of the prepared electrocatalyst was measured by using PANalytical (X'PERT-PRO Powder), (model) with Cu Kα radiation (λ = 0.154 nm). Bi and Ce loading was evaluated by inductively coupled plasma–optical emission spectrometry (ICP-OES) with Thermo Fisher Scientific iCAP 7000 series. The chemical state of the as-obtained materials was examined by an X-ray photoelectron spectrometer (XPS; Axis-Nova, Kratos Inc.) at the Jeonju Center of the Korea Basic Science Institute (KBSI). The determination of the specific surface area and porous properties of the MG and MMGs, nitrogen adsorption-desorption isotherms were measured volumetrically at 77 K (Microtrac, BELsorp-mini II). Product quantification was analyzed via nuclear magnetic resonance spectrometers (^{1}H-NMR) (AVANCE III 400, Bruker, USA) at the Future Energy Convergence Core Center (FECC).

2 Experimental section

2.1 Electrochemical active surface area

Furthermore, the electrochemical active surface area (ECSA) was calculated via the double-layer capacitance (C_{dl}) in the non-Faradaic region and TOF obtained from the formate current density. the electrochemical surface area (ECSA) was determined by the double-layer capacitance method using the equation:

$$ECSA = Cdl/Cs \qquad (1)$$

where C_{dl} is the double-layer capacitance measured by the cyclic voltammetry (CV) method with different scan rates at 5 to 25 mV S^{-1}. The potential is from -0.8 to 1.27 V vs. RHE, and C_{dl} was determined from the plot slope of the double-layer charging current versus the scan rate. C_s is the specific capacitance whose value is 1.12 μF cm^{-2} used in this study.

2.2 Calculation of TOF in H-cell system

TOF and active sites calculation of those Bi_2O_3 electrocatalysts

The formate TOF per site of the Bi_2O_3 catalyst was calculated using the following equations (2):

$$\text{TOF per site} = \frac{\#\ \text{total formate turnovers/cm}^2\ \ \text{geometric area}}{\#\ \text{active sites/cm}^2\ \ \text{geometric area}} \qquad (2)$$

The total number of formate turnovers was estimated by using the following equations (3),

$$\#\ \text{HCOO} = \left(\text{j}\frac{\text{mA}}{\text{cm}^2}\right)\left(\frac{\frac{1\text{C}}{\text{s}}}{1000\ \text{mA}}\right)\left(\frac{1\text{mol e}^-}{96485\ \text{C}}\right)\left(\frac{1\text{mol HCOO}^-}{2\ \text{mol e}^-}\right)\left(\frac{6.022\times10^{23}\text{mol HCOO}^-}{2\text{mol e}}\right)$$

$$= 1.56\times10^{15}\frac{\frac{\text{HCOO}-}{\text{s}}}{\text{cm}^2}\ \text{per}\ \frac{\text{mA}}{\text{cm}^2} \qquad (3)$$

Further, the Ce and Bi, S content of the Bi_2O_3, S-Bi_2O_3, and Ce@S-Bi_2O_3 catalyst was quantified using FE-SEM analysis. The Bi_2O_3 at about ~34.12 wt, Accordingly, the density of active sites based on the Bi, is:

$$\#\ \text{HCOO}- = \left(\frac{34.12}{208.98}\right)\times\frac{1\text{mmol}}{100\ \text{mg}}\times3\frac{\text{mg}}{cm^2}\times6.022\times10^{20}\ \frac{\text{sites}}{\text{mmol}}$$

$$= (0.1632)\times\frac{1\text{mmol}}{100\ \text{mg}}\times3\frac{\text{mg}}{cm^2}\times6.022\times10^{20}\ \frac{\text{sites}}{\text{mmol}}$$

$= 2.94 \times 10^{18}$ sites cm^{-2}

For example, the TOF of the catalyst at -1.16 vs RHE was evaluated below,

$$\text{TOF} = \frac{22.05 \times 3.12 \times 10^{15} \frac{HCOO^-/s}{cm^2}}{2.94 \times 10^{18} \text{ sites cm}^{-2}} = 0.0234 \text{ s}^{-1}$$

TOF and active sites calculation of those S-Bi_2O_3 electrocatalysts

The Formate TOF per site of the S-Bi_2O_3 catalyst was calculated using the following equations (2):

$$\text{TOF per site} = \frac{\#\text{ total formate turnovers/cm}^2 \text{ geometric area}}{\#\text{ active sites/cm}^2 \text{ geometric area}}$$

The total number of formate turnovers was estimated by using the following equations (3),

$$\#\ HCOO = \left(j \frac{mA}{cm^2}\right)\left(\frac{\frac{1C}{s}}{1000\ mA}\right)\left(\frac{1mol\ e^-}{96485\ C}\right)\left(\frac{1mol\ HCOO^-}{2\ mol\ e^-}\right)\left(\frac{6.022 \times 10^{23} mol\ HCOO^-}{2mol\ e}\right)$$

$$= 1.56 \times 10^{15} \frac{\frac{HCOO^-}{s}}{cm^2} \text{ per } \frac{mA}{cm^2} \quad (3)$$

Further, Bi the and S, O content of the S-Bi_2O_3, catalyst was quantified using FE-SEM analysis.

The S-Bi_2O_3 at about ~32.87 wt. Accordingly, the density of active sites based on the Bi is:

$$\#\ HCOO- = \left(\frac{32.87}{208.980}\right) \times \frac{1mmol}{100\ mg} \times 3 \frac{mg}{cm^2} \times 6.022 \times 10^{20} \frac{sites}{mmol}$$

$$= (0.15728) \times \frac{1mmol}{100\ mg} \times 3 \frac{mg}{cm^2} \times 6.022 \times 10^{20} \frac{sites}{mmol}$$

$$= 2.8414 \times 10^{18} \text{ sites cm}^{-2}$$

For example, the TOF of the catalyst at -1.16 vs RHE was evaluated below,

$$\mathrm{TOF} = \frac{27.02 \times 3.12 \times 10^{15} \frac{\mathrm{HCOO^-/s}}{\mathrm{cm^2}}}{2.8414 \times 10^{18}\ \mathrm{sites\ cm^{-2}}} = 0.0296\ \mathrm{s^{-1}}$$

TOF and active sites calculation of those Ce@S-Bi_2O_3 electrocatalysts

The Formate TOF per site of the Ce@S-Bi_2O_3 catalyst was calculated using the following equations (2):

$$\mathrm{TOF\ per\ site} = \frac{\#\ \mathrm{total\ formate\ turnovers/cm^2\ \ geometric\ area}}{\#\ \mathrm{active\ sites/cm^2\ \ geometric\ area}}$$

The total number of formate turnovers was estimated by using the following equations (3),

$$\#\ \mathrm{HCOO} = \left(j \frac{\mathrm{mA}}{cm^2}\right)\left(\frac{\frac{1\mathrm{C}}{\mathrm{s}}}{1000\ \mathrm{mA}}\right)\left(\frac{1\mathrm{mol\ e^-}}{96485\ \mathrm{C}}\right)\left(\frac{1\mathrm{mol\ HCOO^-}}{2\ \mathrm{mol\ e^-}}\right)\left(\frac{6.022 \times 10^{23}\mathrm{mol\ HCOO^-}}{2\mathrm{mol\ e}}\right)$$

$$= 1.56 \times 10^{15} \frac{\frac{\mathrm{HCOO^-}}{\mathrm{s}}}{\mathrm{cm^2}}\ \mathrm{per}\ \frac{\mathrm{mA}}{\mathrm{cm^2}}$$

Further, Ce and Bi the S, O content of the Ce@S-Bi_2O_3, catalyst was quantified using FE-SEM analysis. The Ce@S-Bi_2O_3 at about ~27.62 wt., 2.95 wt. Accordingly, the density of active sites based on the Bi and Ce is:

$$\#\ \mathrm{HCOO-} = \left(\frac{27.62}{208.980} + \frac{2.95}{140.116}\right) \times \frac{1\mathrm{mmol}}{100\ \mathrm{mg}} \times 3 \frac{\mathrm{mg}}{cm^2} \times 6.022 \times 10^{20}\ \frac{\mathrm{sites}}{\mathrm{mmol}}$$

$$= (0.15321) \times \frac{1\mathrm{mmol}}{100\ \mathrm{mg}} \times 3 \frac{\mathrm{mg}}{cm^2} \times 6.022 \times 10^{20}\ \frac{\mathrm{sites}}{\mathrm{mmol}}$$

$$= 2.76789 \times 10^{18}\ \mathrm{sites\ cm^{-2}}$$

For example, the TOF of the catalyst at -1.16 vs RHE was evaluated below,

$$\mathrm{TOF} = \frac{49.9 \times 3.12 \times 10^{15} \dfrac{\mathrm{HCOO^-/s}}{\mathrm{cm^2}}}{2.76789 \times 10^{18}\ \mathrm{sites\ cm^{-2}}} = 0.05624\ \mathrm{s^{-1}}$$

2.3 Product analysis from H-cell system

Liquid phase products were quantified using a ^{1}H-NMR spectrometer (Avance III 400, Bruker, USA) as per previous literature.[2] [3] Initially, the standard calibration curve obtained by measuring NMR readings with different concentration HCOOH with known concentration of internal standard solvent of DMSO (peak at 2.6 ppm). After ECO_2RR, (120 minutes of chronoamperometry analysis with different applied potential) the catholyte solution was collected and analyzed ^{1}H-NMR as follows, 400 µL of catholyte; 120 µL of D_2O; and 10 µL of DMSO. The concentration of produced HCOOH was quantitatively analyzed by integration of the measured peak signal and calculated area ration of DMSO and HCOOH.

$$FE(\%) = \frac{N \times n \times F}{Qtotal} \times 100 \qquad (4)$$

2.4 Computational methodology

All DFT calculations were performed in Vienna ab initio simulation package,[4] using the projector augmented wave pseudopotential using a 400 eV cutoff energy for the valence electrons, and the generalized gradient approximation in the form of Perdew-Burke-Ernzerhof (PBE) for the exchange–correlation potentials.[5] [6] Van der Waals interaction was considered with the DFT-D2 method proposed by Grimme and was used to correct the dispersion 3 forces.[7] The simulation was carried out on a two-dimensional layer and vacuum regions of ≈15 Å along Z-directions to avoid interaction between the layers. The Brillouin zone was sampled by 4 × 4 × 1 for optimization. The various possible active sites were considered for the adsorption of various intermediates such as CO_2, COOH, OCHO, HCOOH, and CO molecules. The computational hydrogen electrode

(CHE) model8 was employed to specify the Gibbs free energy of the proton-electron pair as the function of electrical potential.

The Gibbs free energy change (ΔG) was calculated for the following reaction mechanism and The change in free energy is calculated by the following formula:

$$\Delta G = \Delta E + \Delta E_{ZPE} - T\Delta S \quad (5)$$

Reaction mechanisms for generating formate (6-9), CO (10-13), and H_2 (14-15) were assumed to be

$$cat^* + CO_2 + 2(H^+ + e^-) \leftrightarrow cat^*CO_2 + 2(H^+ + e^-) \quad (6)$$

$$cat^*CO_2 + 2(H^+ + e^-) \leftrightarrow cat^*OCHO + (H^+ + e^-) \quad (7)$$

$$cat^*OCHO + (H^+ + e^-) \leftrightarrow cat^*HCOOH \quad (8)$$

$$cat^*OCHO \leftrightarrow cat^* + HCOOH \quad (9)$$

$$cat^* + CO_2 + 2(H^+ + e^-) \leftrightarrow cat^*CO_2 + 2(H^+ + e^-) \quad (10)$$

$$cat^*CO_2 + 2(H^+ + e^-) \leftrightarrow cat^*COOH + (H^+ + e^-) \quad (11)$$

$$cat^*COOH + (H^+ + e^-) \leftrightarrow cat^*CO + H_2O \quad (12)$$

$$cat^*CO + H_2O \leftrightarrow cat^* + CO + H_2O \quad (13)$$

$$* + H^+ + e^- \leftrightarrow *H \quad (14)$$

$$*H \leftrightarrow * + {}^1/_2 H_2 \quad (15)$$

where cat* represents either a vacant surface catalytic active site or intermediate species adsorbed on the active site.

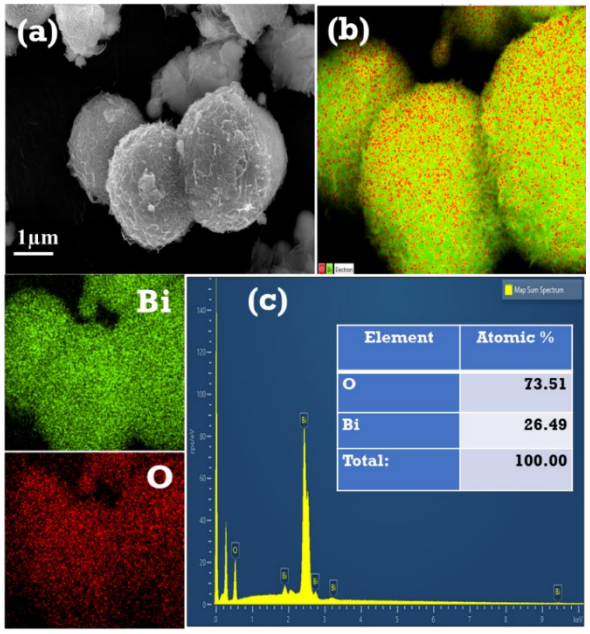

Figure, **S1(a)** illustrates the FESEM image of the Bi_2O_3 structure. **b)** It's certainly revealing the formation of a uniform hierarchical microsphere shape of Bi_2O_3 in the dimension of 3-4 µm. The Bi_2O_3 microsphere structure was homogenously distributed in the overall prepared catalyst. Moreover, the magnified FESEM image confirms the formation of highly porous microspheres with hierarchical nanosheet structures. The corresponding EDS analysis confirms the presence of Bi and O elements in the overall prepared catalyst.

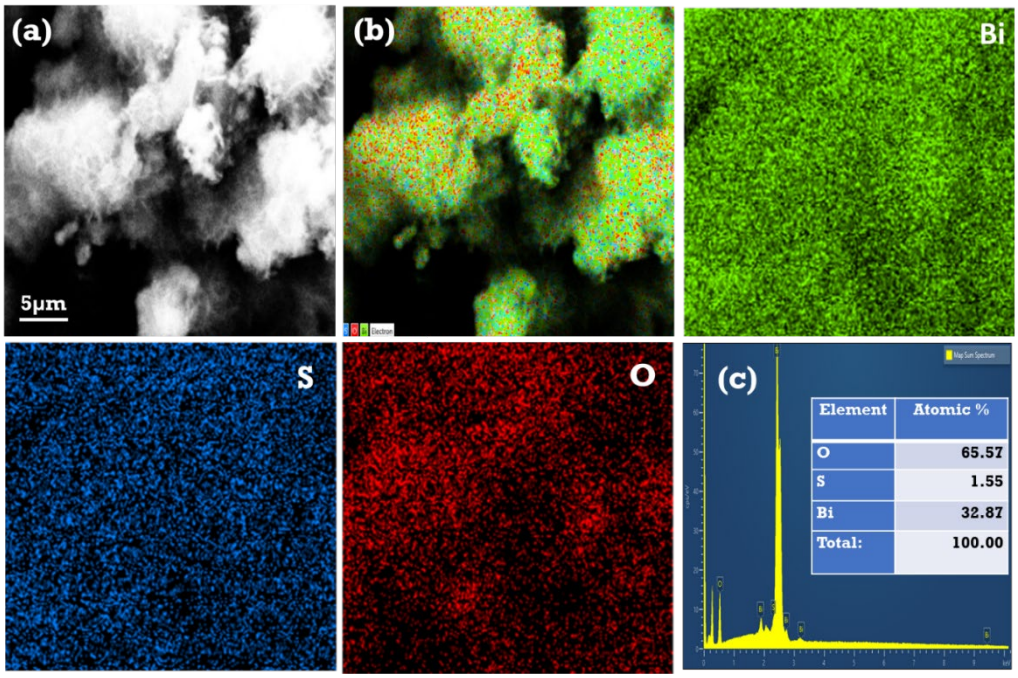

Figure, S2 (a-c) shows FE-SEM images and elemental mapping of sulfur-doped S-Bi_2O_3 nano-structure. After doping with sulfur, there is not much change in the shape of the hierarchical microsphere nanosheets and the morphology of the Bi_2O_3. The corresponding elemental mapping and EDS analysis reveal the uniform doping of sulfur in the overall Bi_2O_3 up to 1.2 at%.

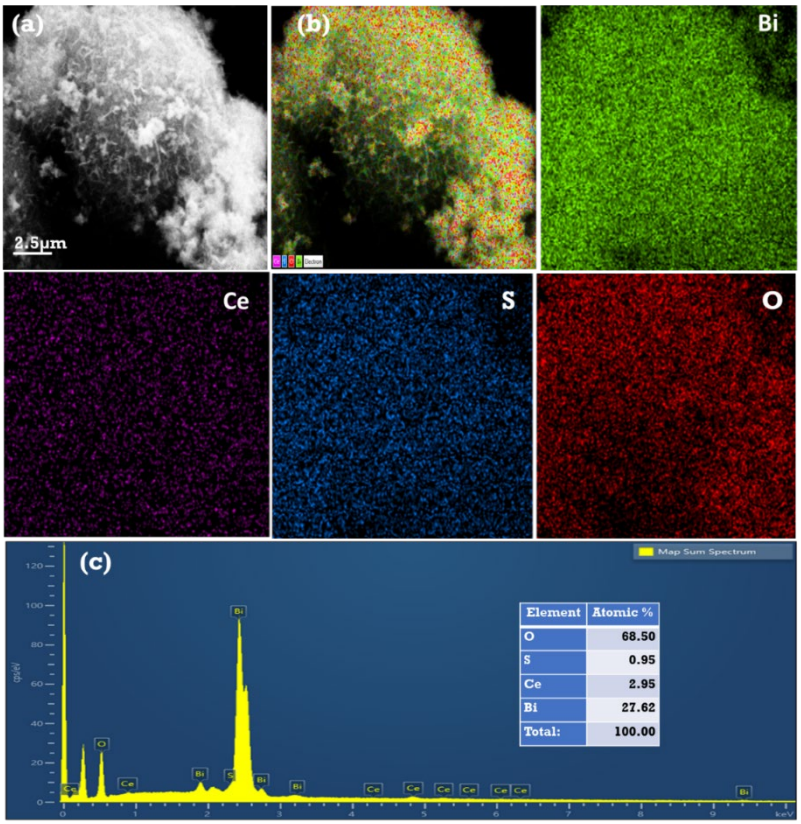

Figure, S3 (a-b) illustrates the FE-SEM micrographs of cerium-doped S-Bi_2O_3 and their corresponding elemental mapping. It confirmed the doping of the cerium atom with S-Bi_2O_3 without delaminating the hierarchical nanosheet morphology of the Bi_2O_3 structure. The corresponding element mapping and EDS analysis show the uniform distribution of elements Bi, Ce, O, and S throughout the catalyst. **c)** represents the low intensities of the S and Ce signals indicating a relatively low content of these elements present in the catalyst.

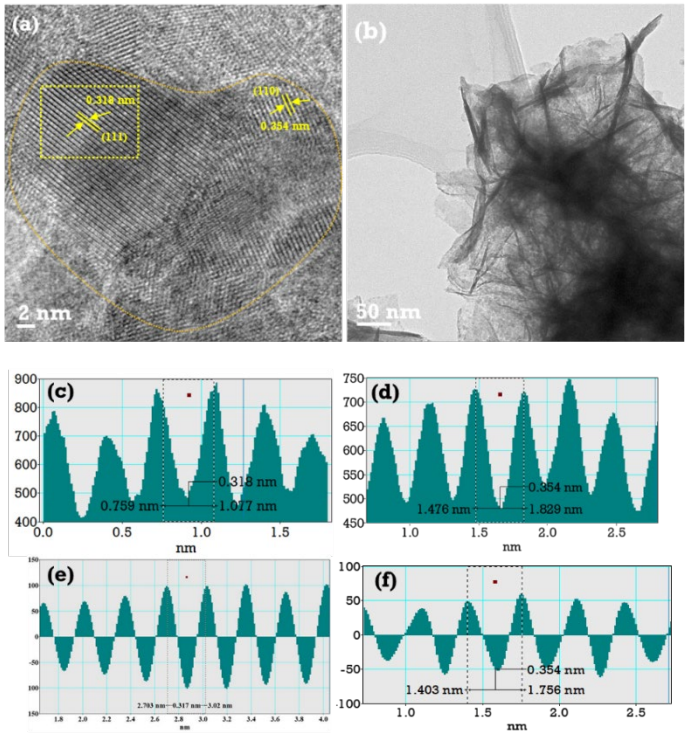

Figure, S4 (**a-b)** HR-TEM and TEM images of Ce@S-Bi_2O_3 hierarchical nanosheets. **(c-f)** reveals the FFT pattern and IFFT pattern of the corresponding catalyst for ECO_2RR.

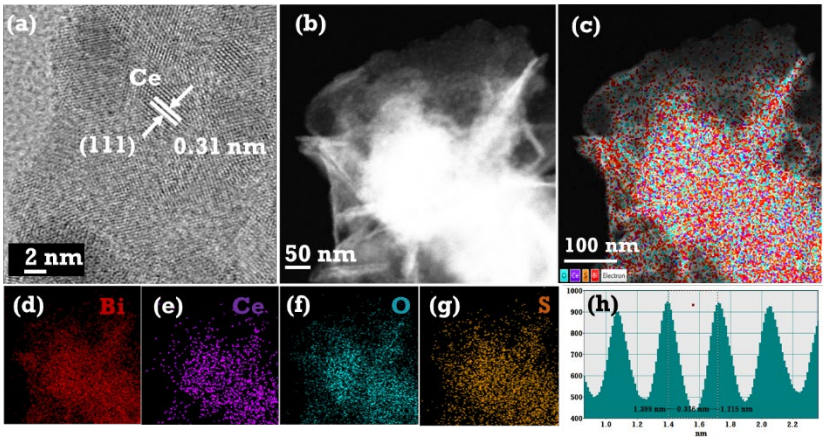

Figure, S5 (a-b) illustrates the HAADF-STEM, and elemental color mapping of Ce@S-Bi_2O_3 hierarchical nanosheets. **(c-h)** The overall elemental mapping and corresponding EDS elemental mapping with FFT image**.**

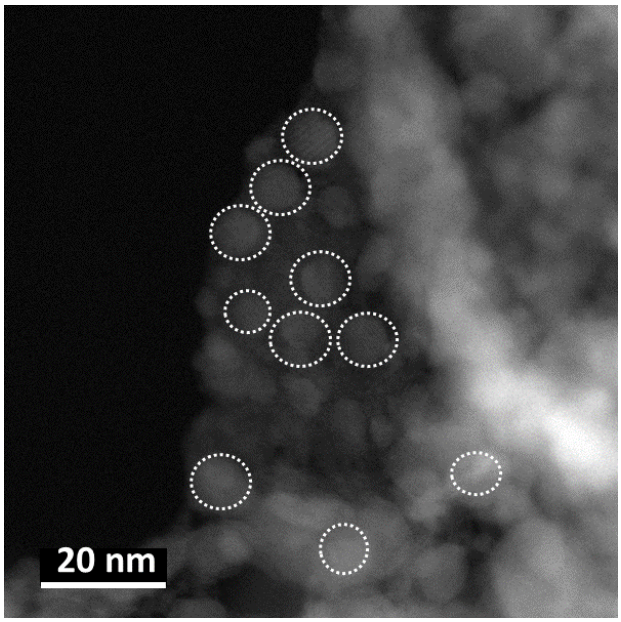

Figure, S6 illustrates the (HAADF-STEM) of Ce@S-Bi_2O_3, it further identifies the structure of Bi nanosheets showing that the nanoparticles are making well-defined flexible hierarchical nanosheets appear.

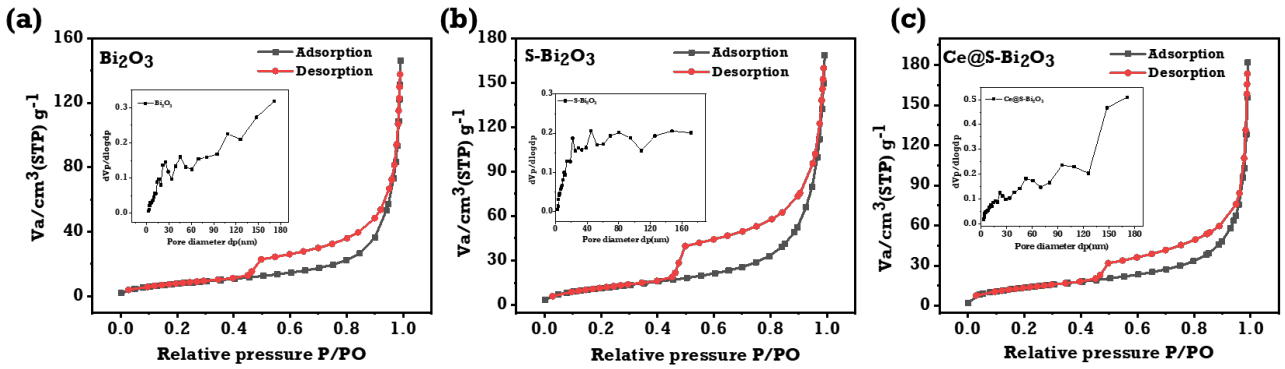

Figure, S7 (a-c) Nitrogen adsorption - desorption isotherms and pore size distributions of Bi_2O_3, S-Bi_2O_3, and Ce@S-Bi_2O_3 electrocatalyst.

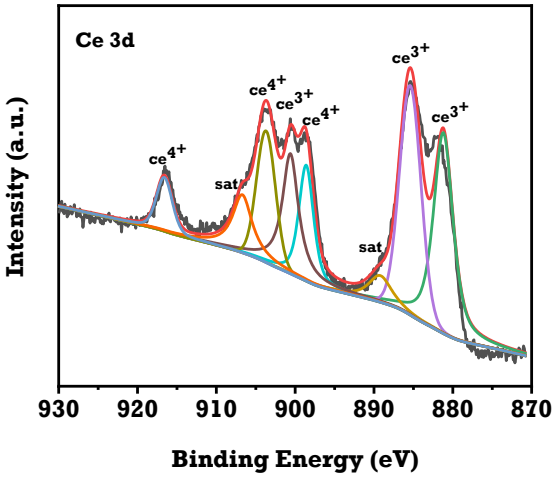

Figure, S8 represents the XPS spectrum of core Ce 3d.

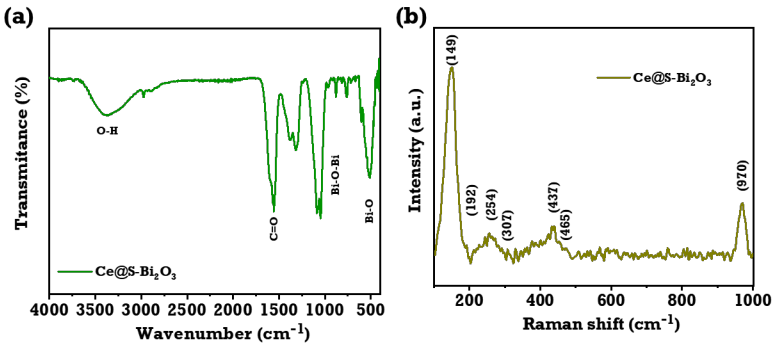

Figure, S9 (a-b) the FT-IR and Raman spectrum of Ce@S-Bi_2O_3 electrocatalyst

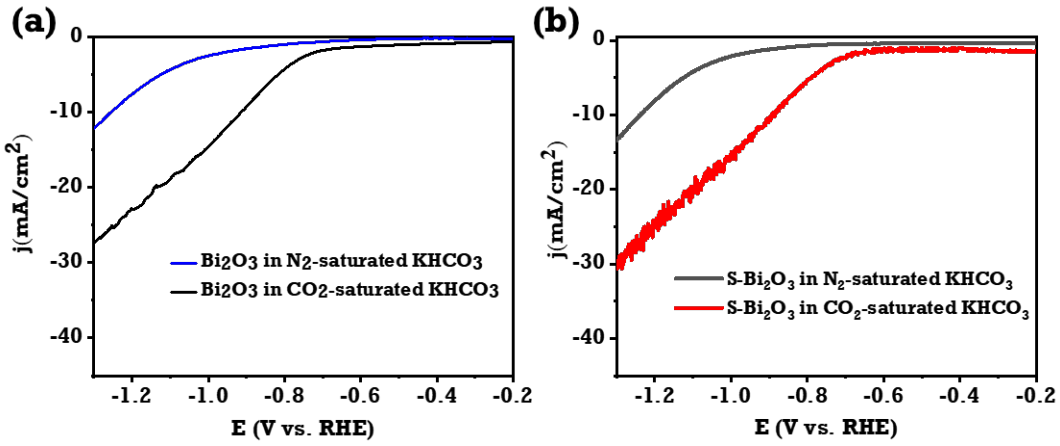

Figure, S10 (a-b) shows a LSV curve of obtained Bi_2O_3, S-Bi_2O_3, and Ce@S-Bi_2O_3 electrocatalyst.

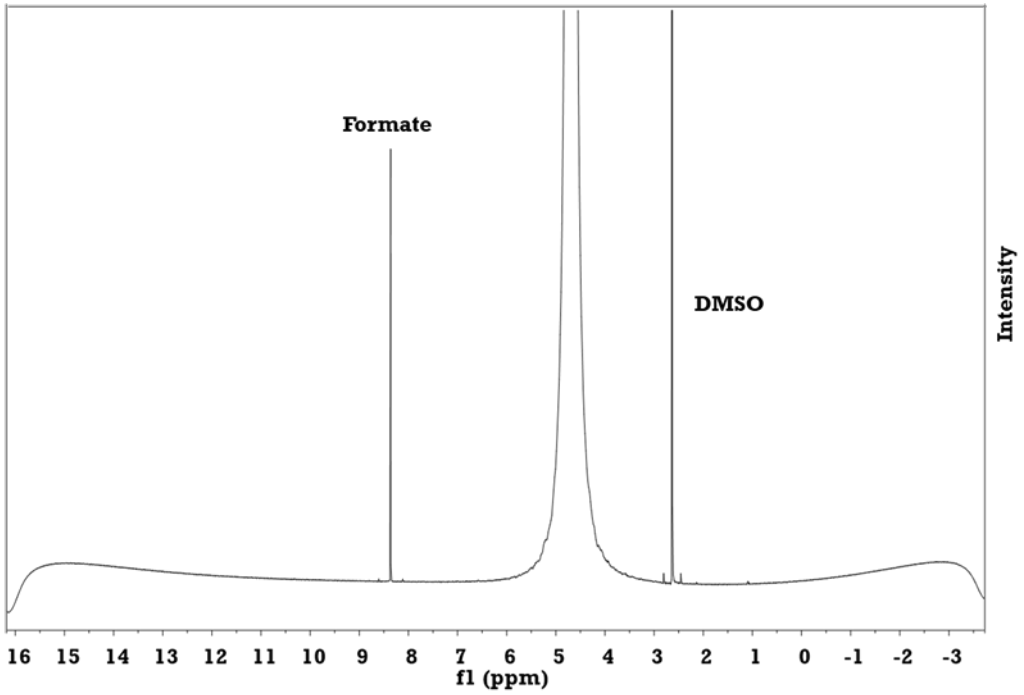

Figure, S11 ^{1}H-NMR analysis of formate with DMSO as an internal standard obtained from the Ce@S-Bi_2O_3 electrocatalyst.

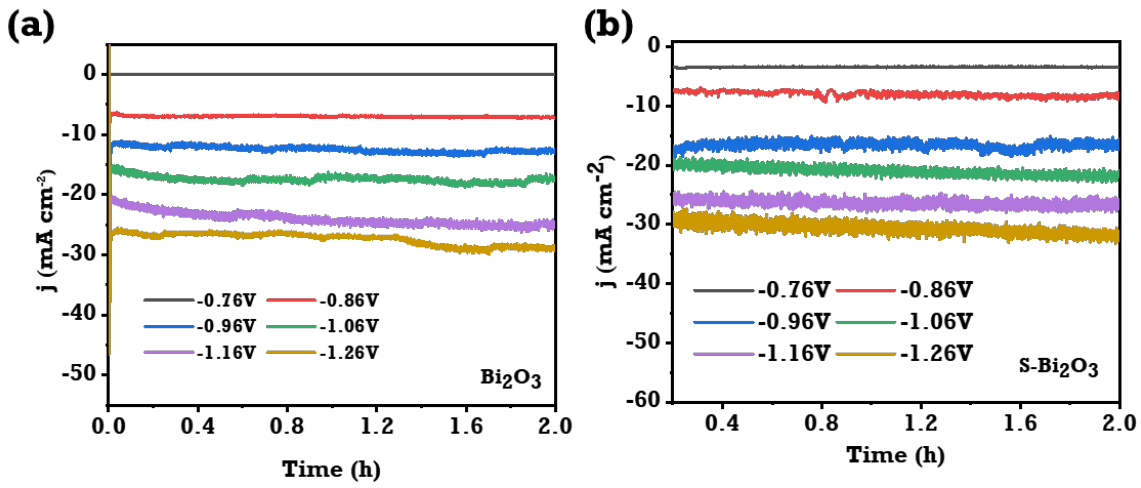

Figure, S12 (a-b) shows the chronoamperometry of corresponding electrocatalysts of Bi_2O_3 and S-Bi_2O_3.

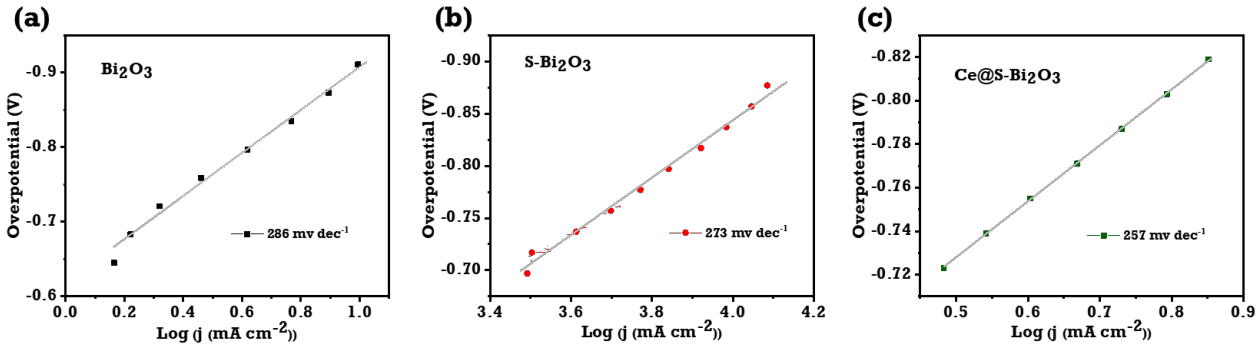

Figure, S13 (**a-c)** Tafel slope of Bi_2O_3, S-Bi_2O_3, and Ce@S-Bi_2O_3 electrocatalysts.

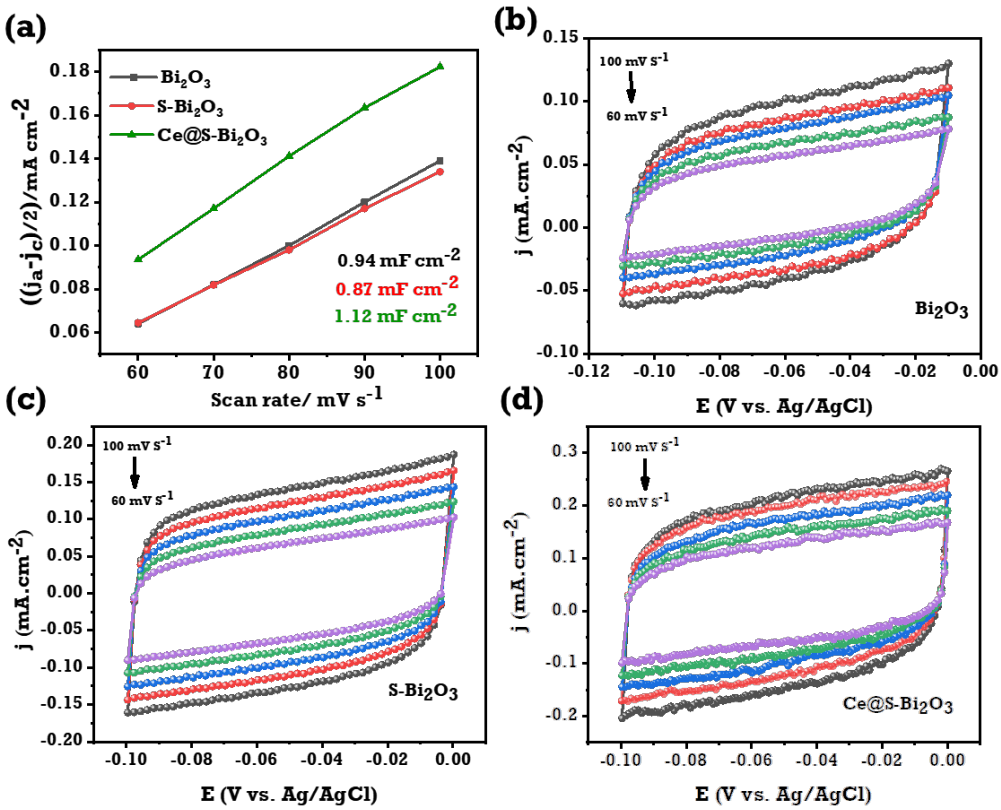

Figure, S14 (a-d) Double layer capacitance (C_{dl}) measurements curve of Bi_2O_3, S-Bi_2O_3, and Ce@S-Bi_2O_3 electrocatalysts.

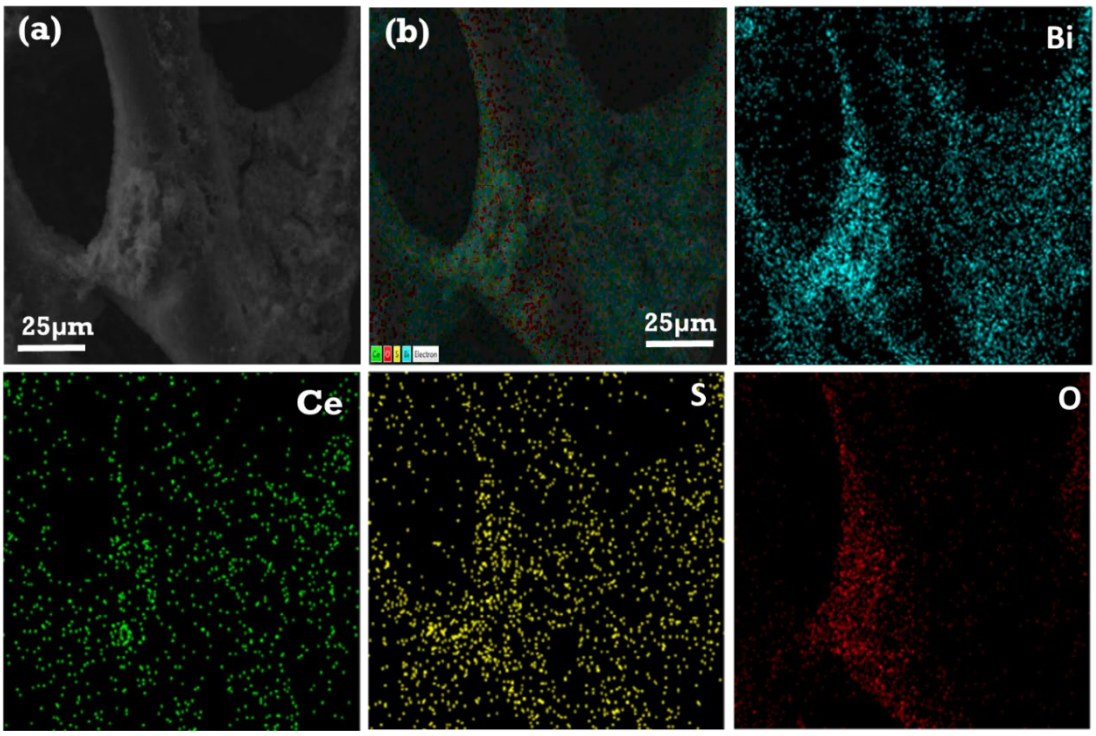

Figure, S15(a) After the ECO_2RR the FE-SEM images show a Ce@S-Bi_2O_3 catalyst. **(b)** reveals the overlap of catalysts in the present electrode areas and the evidence of respective EDS elemental mapping of the catalysts was presents Bi, Ce, S, O the corresponding elemental mapping.

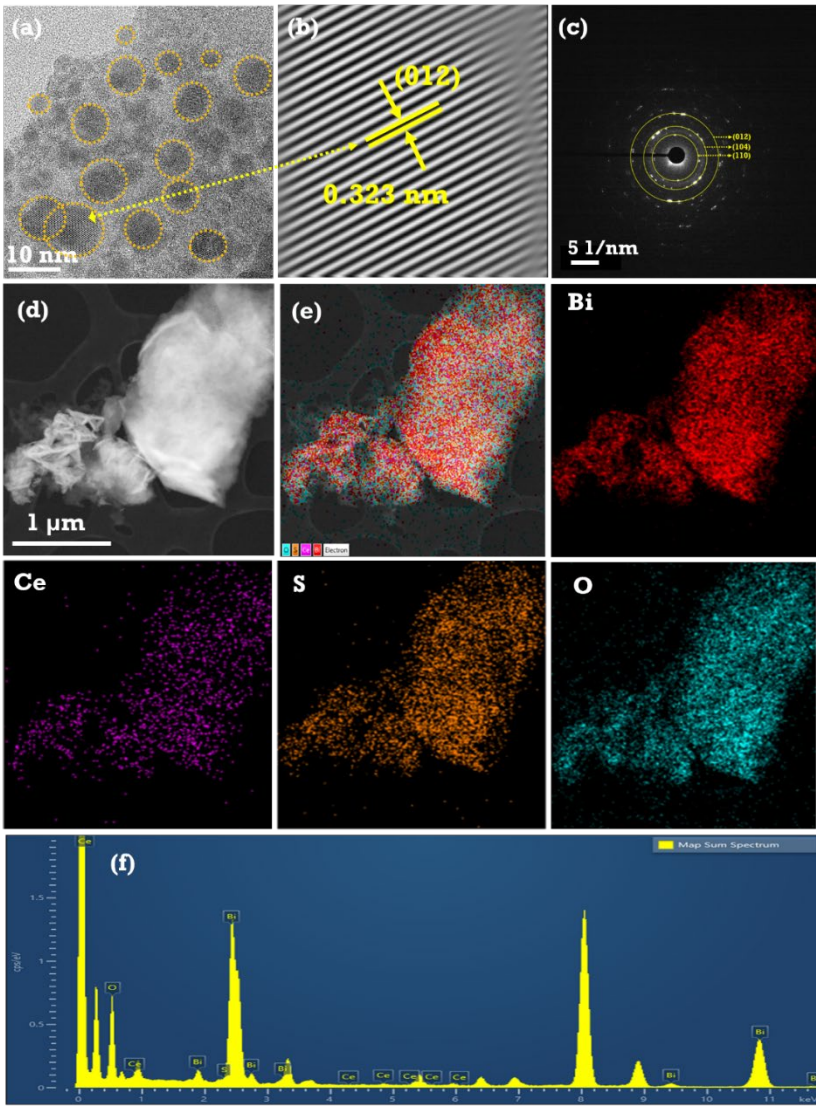

Figure, S16 (a-c) represents the HRTEM images of Ce@S-Bi_2O_3 and the corresponding d-spacing plane and SAED patterns with crystal planes. (**d-f)** shows the HR-TEM image and the corresponding EDS mapping spectrum after the ECO_2RR performance.

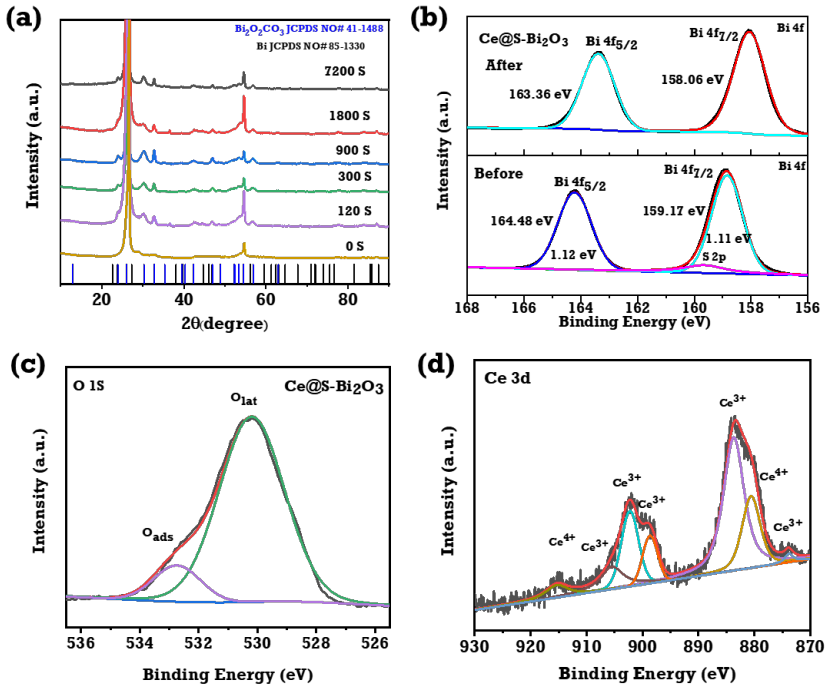

Figure, S17 (a) Time-dependent XRD curve of the Ce@S-Bi_2O_3 electrocatalyst during the ECO_2RR. (**b-d)** Before and after (2 h) electrochemical CO_2RR shows the XPS spectra of Bi4f and O1s, Ce 3d survey spectrum of Ce@S-Bi_2O electrocatalysts.

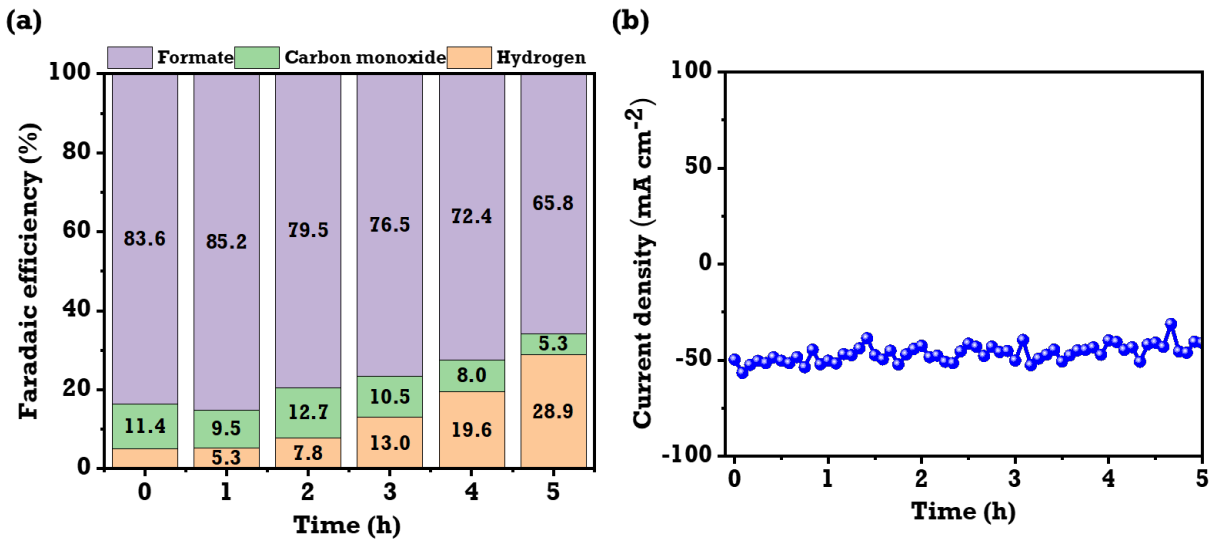

Figure S18 (a) Faradaic efficiency, **(b)** current density of Ce@S-Bi_2O_3 at -1.2 V vs RHE during the continuous stability test up to 5 hours.

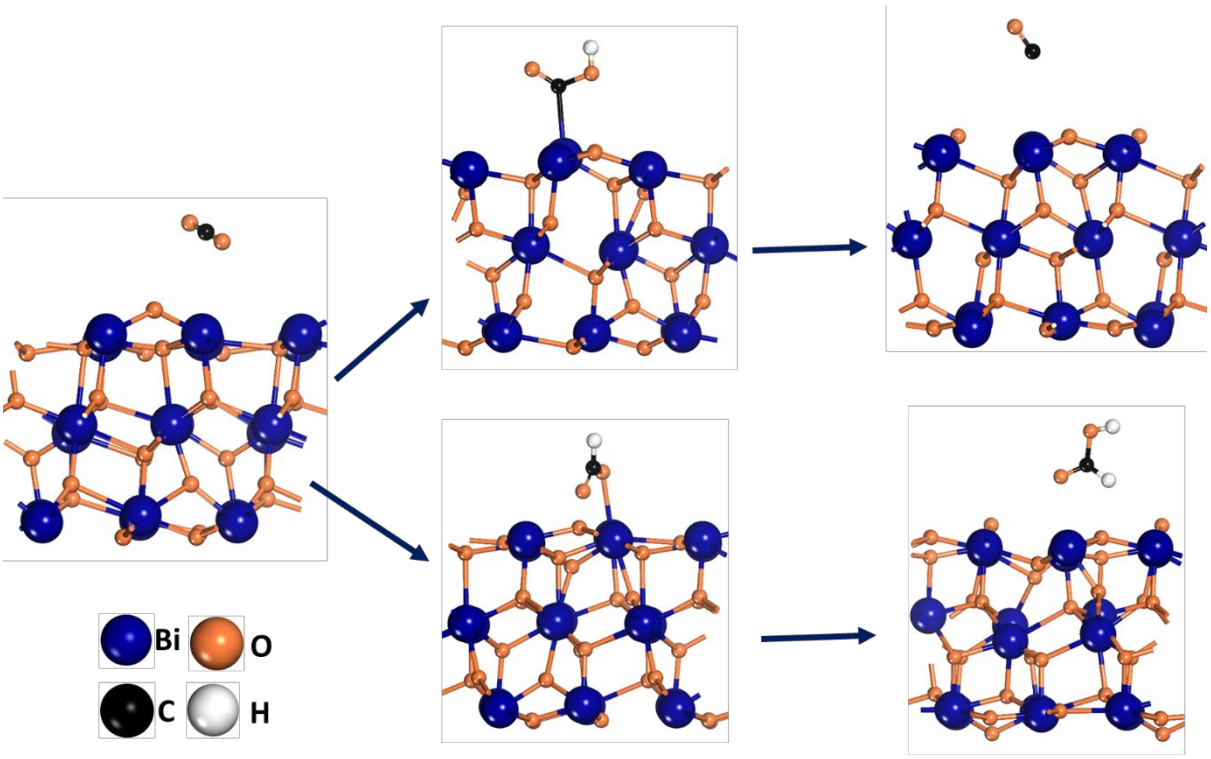

Figure, S19 Optimized configurations of *CO_2, *COOH, *CO, *OCHO, and *HCOOH on (111) planes of Bi_2O_3.

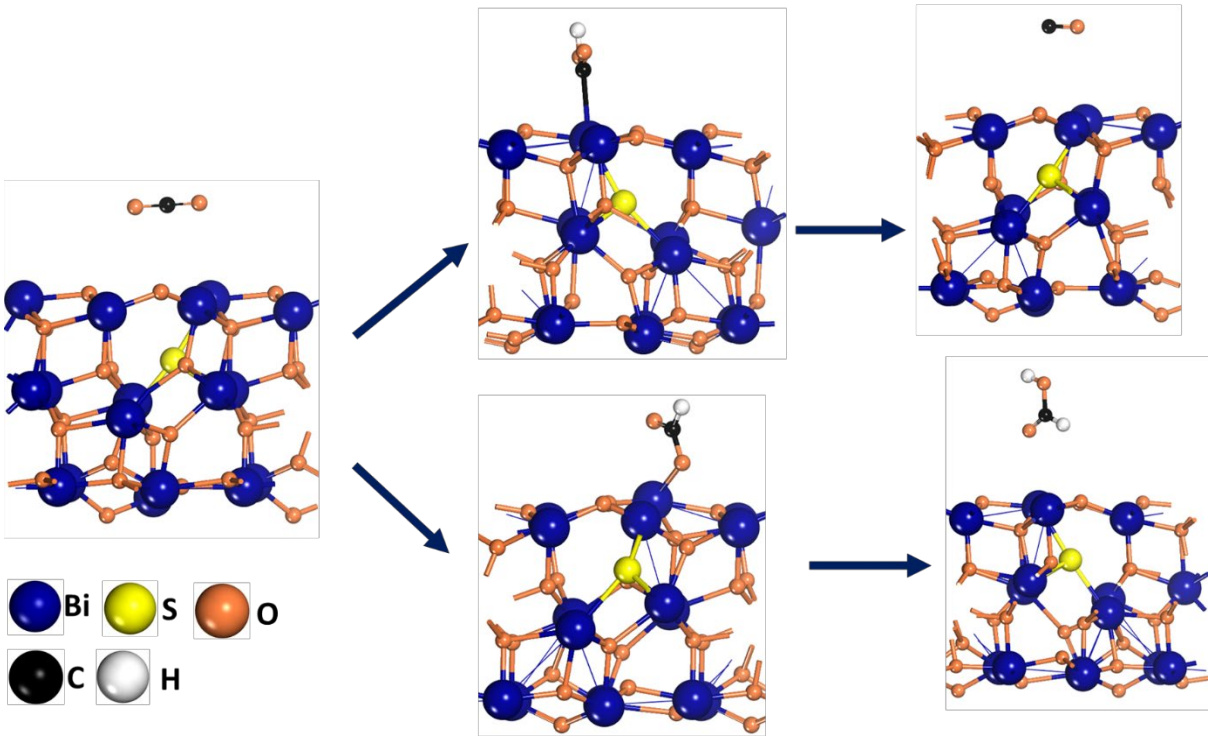

Figure, S20 Optimized configurations of *CO_2, *COOH, *CO, *OCHO, and *HCOOH on (111) planes of S doped on Bi_2O_3.

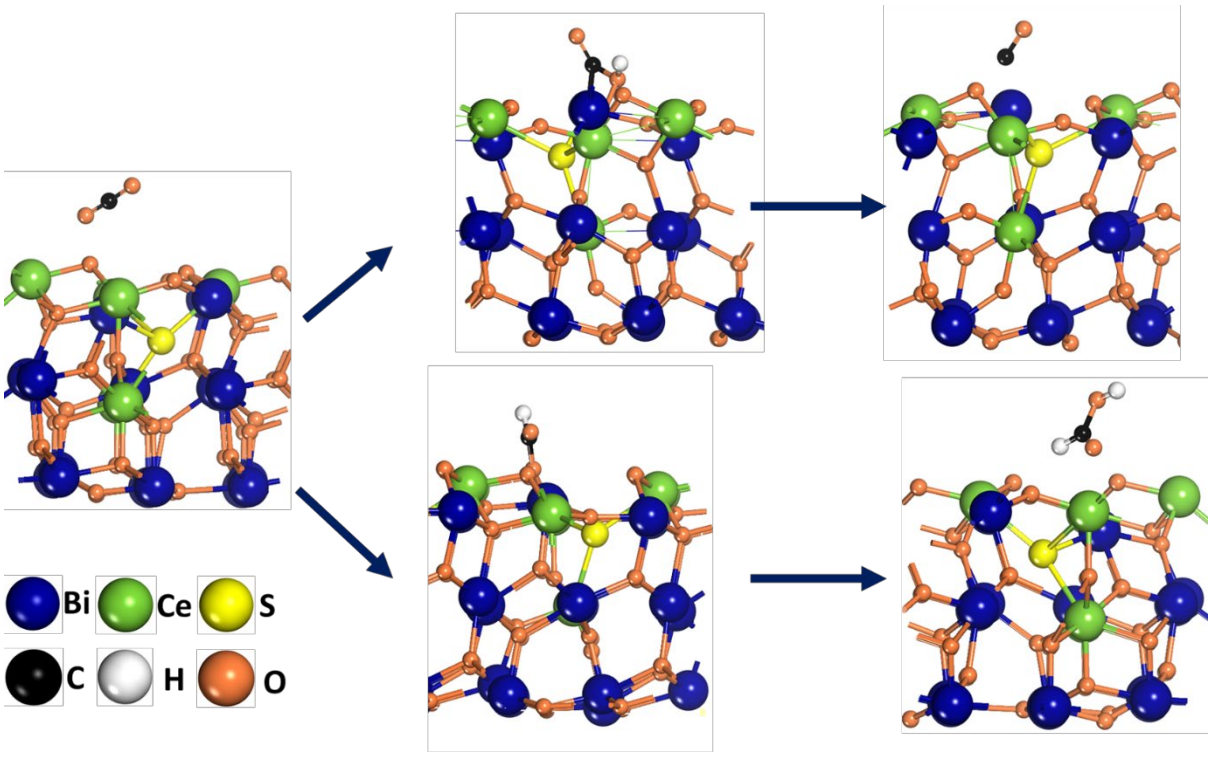

Figure, S21 Optimized configurations of *CO_2, *COOH, *CO, *OCHO, and *HCOOH on (111) planes of Ce@S-doped on Bi_2O_3 (On top of Bi).

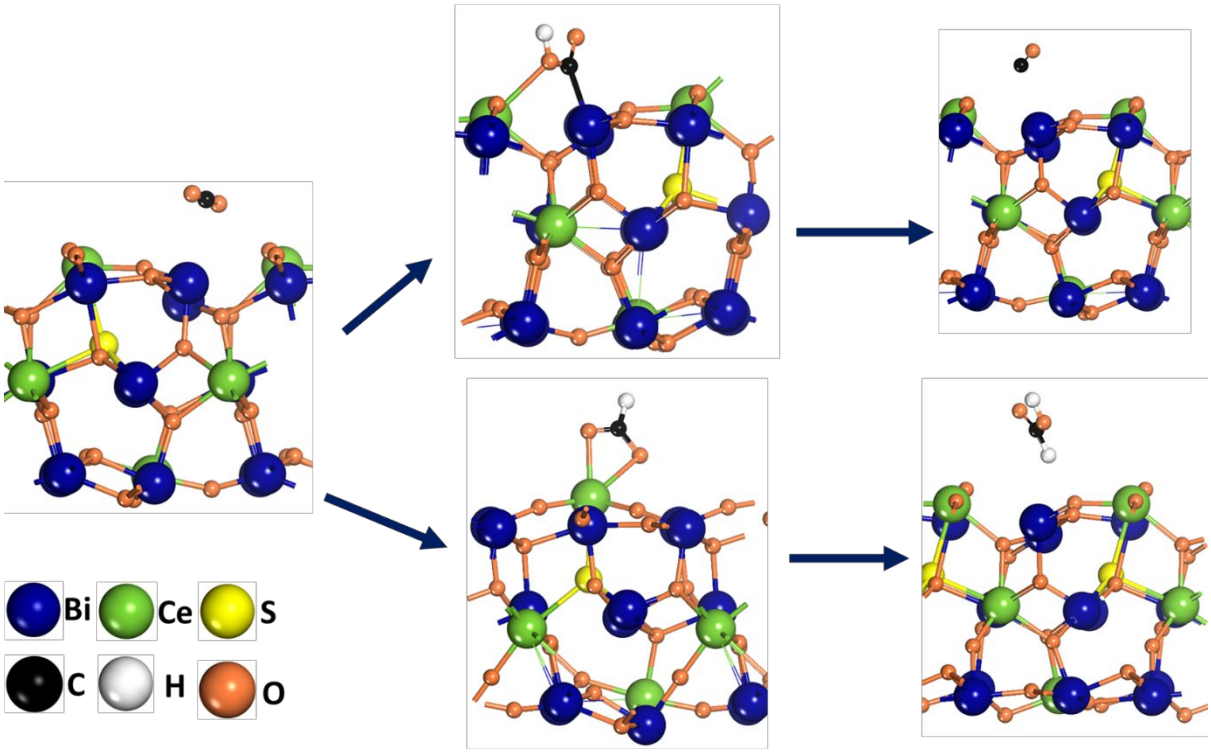

Figure, S22 Optimized configurations of *CO_2, *COOH, *CO, *OCHO, and *HCOOH on (111) planes of Ce@S-doped on Bi_2O_3 (On top of Ce).

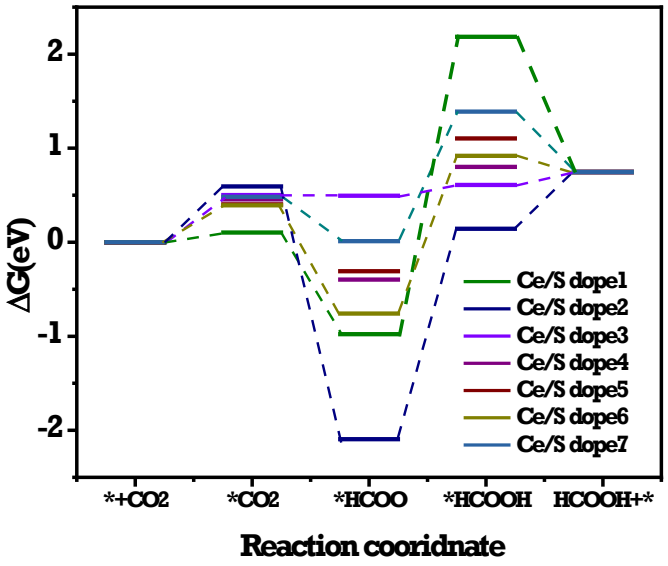

Figure, S23 shows several models for Ce and S doping in Bi_2O_3

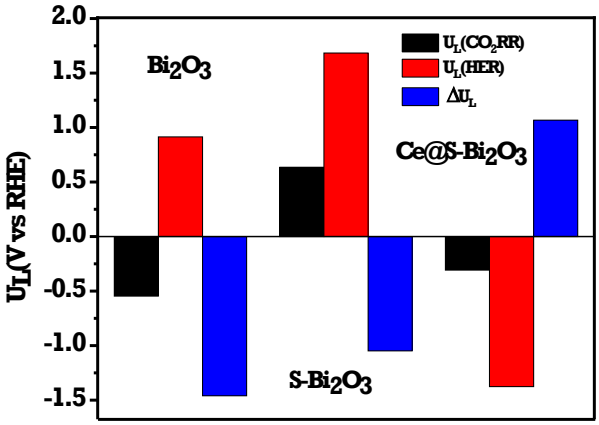

Figure, S24 Limiting potential difference between CO_2RR and HER for Bi_2O_3, S-Bi_2O_3, and Ce@S-Bi_2O_3 at each site.

Table S1: BET surface area, pore volume, and diameter of electrocatalysts

Materials	BET surface area (m^2 g^{-1})	Pore volume (cm^3 g^{-1})	Pore diameter (nm)
Bi_2O_3	30.403	0.2129	28.005
S-Bi_2O_3	44.019	0.2447	22.232
Ce@S-Bi_2O_3	50.482	0.2716	21.522

Table S2: The ICP-OES results of Ce@S-Bi_2O_3 (At. %) electrocatalyst before and after ECO_2RR.

Ce@S-Bi_2O_3 Electrocatalyst	Bi (At. %)	Ce (At. %)	S (At. %)
Before ECO_2RR	27.8	3.3	1.2
After ECO_2RR	17.0	2.5	0.8

Table S3: Gibbs free energy changes (ΔG) in the reaction steps formation of HCOOH

materials	ΔG1(*CO_2)	ΔG2(*OCHO)	ΔG3(*HCOOH)
Bi_2O_3	-1.52099	-0.54595	-1.87043
S-Bi_2O_3	0.19033	0.63571	0.14487
Ce/S- Bi_2O_3	0.50134	0.49527	0.60952
Ce/S- Bi_2O_3	0.4032	-0.3081	1.10412

Table S4: Gibbs free energy changes (ΔG) in the reaction steps formation of CO

materials	ΔG1(*CO_2)	ΔG2(*COOH)	ΔG3(*CO)
Bi_2O_3	-1.52099	1.03843	-0.05979
S-Bi_2O_3	0.19033	2.72785	0.79759
Ce/S- Bi_2O_3	0.50134	1.8057	2.3497
Ce/S- Bi_2O_3	0.4032	1.65222	2.22612

Table S5: Gibbs free energy changes (ΔG) in the reaction steps formation of HCOOH for Ce/S doping in Bi_2O_3

materials	ΔG1(*CO_2)	ΔG2(*OCHO)	ΔG3(*HCOOH)
Ce/S- dope1	0.10336	-0.9782	2.18534
Ce/S- dope2	0.59413	-2.09397	0.14357
Ce/S- dope3	0.50134	0.49527	0.60952
Ce/S- dope4	0.45647	-0.3976	0.80099
Ce/S- dope5	0.4032	-0.3081	1.10412
Ce/S- dope6	0.39233	-0.75867	0.91896
Ce/S- dope7	0.48238	0.01174	1.38861

Table S6: Performance comparison of various Bi-electrocatalyst ECO_2 RR in H-cell.

Materials	**Cell configuration**	**electrolyte**	**Potential (V vs. RHE)**	**$J_{formate}$ ($mA\ cm^{-2}$)**	**$FE_{formate}$**	**Ref**
Ce@S-Bi_2O_3	**H-cell**	**0.5 M $KHCO_3$**	**-1.16**	**±42.09**	**± 92.5%**	**This work**
Bi /Bi_2O_3-CP	H-cell	0.5 M $KHCO_3$	-1.17	72	90.4	[8]
Cux-Bi/Bi_2O_3@C	H-cell	0.5 M $KHCO_3$	-0.94	10.1	93	[9]
Bi-NAs	H-cell	0.5 M $KHCO_3$	-0.95	45	90	[10]
Bi /Bi_2O_3	H-cell	0.5 M $KHCO_3$	-1.3	87.14	90	[11]
Bi-PVP/CC600	H-cell	0.5 M $KHCO_3$	-0.83	54	86	[12]
Bi-MOF	Home-made three-electrode cell	0.5 M $KHCO_3$	-0.9	41.0	92.2	[13]
OD-BiNSs	H-cell	0.5 M $KHCO_3$	-0.95	62	93	[14]
Bi nanostructure	H-cell	0.5 M $KHCO_3$	-0.9	18	92	[15]
$Bi_2O_2CO_3$	H-cell	0.5M $NaHCO_3$	-0.7	11	95	[16]
Bi nanotubes	H-cell	0.1M $KHCO_3$	-1.0	22	95	[17]
Bi_2S_3-Bi_2O_3@rGO	H-cell	0.5M $KHCO_3$	-0.9	3.5	90	[18]
Bi-Sn/CF	H-cell	0.5M $KHCO_3$	-1.14	43.2	96	[19]
S- Bi_2O_3-CNT	H-cell	0.5M $KHCO_3$	-0.9	28.17	97.06	[20]
Bi_2O_3@C	H-cell	0.5M $KHCO_3$	-0.9	7.5	92	[21]
Bi_2O_3 NP	H-cell	0.5M $KHCO_3$	-0.83	3.4	92	[22]

Reference:

[1] T. Chatterjee, E. Boutin, M. Robert, *Dalton Transactions* **2020**, 49, 4257.

[2] C. S. Chen, A. D. Handoko, J. H. Wan, L. Ma, D. Ren, B. S. Yeo, *Catalysis Science & Technology* **2015**, 5, 161.

[3] D. Ren, J. Gao, L. Pan, Z. Wang, J. Luo, S. M. Zakeeruddin, A. Hagfeldt, M. Grätzel, *Angewandte Chemie International Edition* **2019**, 58, 15036.

[4] a) G. Kresse, J. Furthmüller, *Computational Materials Science* **1996**, 6, 15

b) G. Kresse, J. Furthmüller, *Physical Review B* **1996**, 54, 11169.

[5] J. P. Perdew, M. Ernzerhof, K. Burke, *The Journal of Chemical Physics* **1996**, 105, 9982.

[6] J. P. Perdew, K. Burke, M. Ernzerhof, *Physical Review Letters* **1996**, 77, 3865.

[7] S. Grimme, *Journal of Computational Chemistry* **2006**, 27, 1787.

[8] D. Wu, G. Huo, W. Y. Chen, X. Z. Fu, J. L. Luo, *Applied Catalysis B: Environmental* **2020**, 271, 118957.

[9] Y. Xue, C. Li, X. Zhou, Z. Kuang, W. Zhao, Q. Zhang, H. Chen, *ChemElectroChem* **2022**, 9, e202101648.

[10] J. Fan, X. Zhao, X. Mao, J. Xu, N. Han, H. Yang, B. Pan, Y. Li, L. Wang, Y. Li, *Advanced Materials* **2021**, 33, 2100910.

[11] W. Wang, G. Ruan, X. Wang, C. Wu, Q. Wang, *New Journal of Chemistry* **2023**, 47, 8894.

[12] D. Wu, X. Wang, X.Z. Fu, J.L. Luo, *Applied Catalysis B: Environmental* **2021**, 284, 119723.

[13] F. Li, G. H. Gu, C. Choi, P. Kolla, S. Hong, T.S. Wu, Y.L. Soo, J. Masa, S. Mukerjee, Y. Jung, J. Qiu, Z. Sun, *Applied Catalysis B: Environmental* **2020**, 277, 119241.

[14] J. Lee, H. Liu, Y. Chen, W. Li, *ACS Applied Materials & Interfaces* **2022**, 14, 14210.

[15] P. Lu, D. Gao, H. He, Q. Wang, Z. Liu, S. Dipazir, M. Yuan, W. Zu, G. Zhang, *Nanoscale* **2019**, 11, 7805.

[16] Y. Zhang, X. Zhang, Y. Ling, F. Li, A. M. Bond, J. Zhang, *Angewandte Chemie International Edition* **2018**, 57, 13283.

[17] K. Fan, Y. Jia, Y. Ji, P. Kuang, B. Zhu, X. Liu, J. Yu, *ACS Catalysis* **2020**, 10, 358.

[18] X. Yang, P. Deng, D. Liu, S. Zhao, D. Li, H. Wu, Y. Ma, B. Y. Xia, M. Li, C. Xiao, S. Ding, *Journal of Materials Chemistry A* **2020**, 8, 2472.

[19] G. Wen, D. U. Lee, B. Ren, F. M. Hassan, G. Jiang, Z. P. Cano, J. Gostick, E. Croiset, Z. Bai, L. Yang, Z. Chen, *Advanced Energy Materials* **2018**, 8, 1802427.

[20] S.Q. Liu, M.-R. Gao, R.F. Feng, L. Gong, H. Zeng, J.L. Luo, *ACS Catalysis* **2021**, 11, 7604.

[21] P. Deng, F. Yang, Z. Wang, S. Chen, Y. Zhou, S. Zaman, B. Y. Xia, *Angewandte Chemie International Edition* **2020**, 59, 10807.

[22] C.C. Miao, G.Q. Yuan, *ChemElectroChem* **2018**, 5, 3741.